



UNSTEADY TRANSONIC FLOW OVER BLUNT AND POINTED BODIES OF REVOLUTION

T. Hsieh

ARO, Inc., a Sverdrup Corporation Company

**PROPULSION WIND TUNNEL FACILITY
ARNOLD ENGINEERING DEVELOPMENT CENTER
AIR FORCE SYSTEMS COMMAND
ARNOLD AIR FORCE STATION, TENNESSEE 37389**

February 1978

Final Report for Period 1 July 1975 – 13 April 1977

Approved for public release; distribution unlimited.

Prepared for

**ARNOLD ENGINEERING DEVELOPMENT CENTER/DOTR
ARNOLD AIR FORCE STATION, TENNESSEE 37389**

NOTICES

When U. S. Government drawings, specifications, or other data are used for any purpose other than a definitely related Government procurement operation, the Government thereby incurs no responsibility nor any obligation whatsoever, and the fact that the Government may have formulated, furnished, or in any way supplied the said drawings, specifications, or other data, is not to be regarded by implication or otherwise, or in any manner licensing the holder or any other person or corporation, or conveying any rights or permission to manufacture, use, or sell any patented invention that may in any way be related thereto.

Qualified users may obtain copies of this report from the Defense Documentation Center.

References to named commercial products in this report are not to be considered in any sense as an indorsement of the product by the United States Air Force or the Government.

This report has been reviewed by the Information Office (OI) and is releasable to the National Technical Information Service (NTIS). At NTIS, it will be available to the general public, including foreign nations.

APPROVAL STATEMENT


This report has been reviewed and approved.



ELTON R. THOMPSON
Project Manager, Research Division
Directorate of Test Engineering

Approved for publication:

FOR THE COMMANDER



MARION L. LASTER
Director of Test Engineering
Deputy for Operations

UNCLASSIFIED

REPORT DOCUMENTATION PAGE		READ INSTRUCTIONS BEFORE COMPLETING FORM
1 REPORT NUMBER AEDC-TR-77-100	2 GOVT ACCESSION NO.	3. RECIPIENT'S CATALOG NUMBER
4. TITLE (and Subtitle) UNSTEADY TRANSONIC FLOW OVER BLUNT AND POINTED BODIES OF REVOLUTION		5 TYPE OF REPORT & PERIOD COVERED Final Report, 1 July 1975 - 13 April 1977
		6. PERFORMING ORG. REPORT NUMBER
7 AUTHOR(s) T. Hsieh, ARO, Inc.		8 CONTRACT OR GRANT NUMBER(s)
9 PERFORMING ORGANIZATION NAME AND ADDRESS Arnold Engineering Development Center Air Force Systems Command Arnold Air Force Station, TN 37389		10. PROGRAM ELEMENT, PROJECT, TASK AREA & WORK UNIT NUMBERS Program Element 65807F
11 CONTROLLING OFFICE NAME AND ADDRESS Arnold Engineering Development Center/DOS Air Force Systems Command Arnold Air Force Station, TN 37389		12. REPORT DATE February 1978
		13. NUMBER OF PAGES 47
14 MONITORING AGENCY NAME & ADDRESS (if different from Controlling Office)		15. SECURITY CLASS. (of this report) UNCLASSIFIED
		15a. DECLASSIFICATION/DOWNGRADING SCHEDULE N/A
16 DISTRIBUTION STATEMENT (of this Report) Approved for public release; distribution unlimited.		
17 DISTRIBUTION STATEMENT (of the abstract entered in Block 20, if different from Report)		
18 SUPPLEMENTARY NOTES Available in DDC.		
19 KEY WORDS (Continue on reverse side if necessary and identify by block number) perturbation theory ellipse cylinder bodies of revolution parabolic arc nose oscillation hemisphere-cylinder		
20 ABSTRACT (Continue on reverse side if necessary and identify by block number) A perturbation theory and numerical solution, based on the unsteady full potential equation, were developed to calculate the unsteady transonic flow field over blunt and pointed bodies of revolution performing harmonic oscillatory motions at zero incidence. Calculations were performed for pulsatile oscillations for a hemisphere-cylinder and pitching oscillations for an ogive-cylinder, an ellipse-cylinder, a hemisphere-cylinder, and a parabolic arc nose. Comparison between theory and experiments was made for the surface pressure distribution at quasi-steady state and for the static and dynamic stability derivatives.		

UNCLASSIFIED

PREFACE

The work presented herein was conducted by the Arnold Engineering Development Center (AEDC), Air Force Systems Command (AFSC), under Program Element 65807F. The Air Force project manager was Mr. Elton Thompson (AEDC/DOTR). The results presented were obtained by ARO, Inc., AEDC Division (a Sverdrup Corporation Company), operating contractor for the AEDC, AFSC, Arnold Air Force Station, Tennessee, under ARO Project Numbers P32A-C2A and P33A-K0A. Analysis of the results was completed in June 1977, and the manuscript (ARO Control No. ARO-PWT-TR-77-64) was submitted for publication on September 30, 1977.

CONTENTS

	<u>Page</u>
1.0 INTRODUCTION	5
2.0 ANALYSIS	
2.1 Basic Equations	5
2.2 Boundary Conditions	9
2.3 Pressure Coefficients	9
3.0 COMPUTATIONAL SCHEME	
3.1 Difference Equations	11
3.2 Boundary Conditions	14
4.0 RESULTS AND DISCUSSION	
4.1 General Remarks	16
4.2 Pulsatile Oscillation	16
4.3 Pitching Oscillation	17
5.0 CONCLUDING REMARKS	37
REFERENCES	37

ILLUSTRATIONS

Figure

1. Body-Normal Coordinate System	7
2. Transformation from Physical to Computational Plane	10
3. The Neighboring Points Used in the Difference Scheme	12
4. Quasi-Steady Surface Pressure Perturbation for Hemisphere-Cylinder at $M_\infty = 0.6$	17
5. Quasi-Steady Surface Pressure Perturbation for Hemisphere-Cylinder at $M_\infty = 1.2$	18
6. Comparison of Steady-State Surface Pressure Between Theory and Experiments for a 4-Caliber Ogive-Nose-Cylinder	19
7. Comparison of Quasi-Steady Perturbed Surface Pressure Between Theory and Experiments for a 4-Caliber Ogive-Nose-Cylinder	19
8. Comparison of Steady-State Surface Pressure Between Theory and Experiments for a 2:1 Ellipse-Nose-Cylinder	20
9. Comparison of Quasi-Steady Perturbed Surface Pressure Between Theory and Experiments for a 2:1 Ellipse-Nose-Cylinder	21

<u>Figure</u>	<u>Page</u>
10. Comparison of Quasi-Steady Perturbed Surface Pressure Between Theory and Experiments for a Hemisphere-Cylinder	23
11. Shadowgraphs of Hemisphere-Cylinder at 5 deg	25
12. Comparison of Surface Pressure Between Theory and Experiments for a 2:1 Ellipse-Nose-Cylinder at Incidence and $M_\infty = 0.9$	26
13. Comparison of Static Stability Derivatives Between Theory and Experiments for a 2-Caliber Ogive-Nose-Cylinder	27
14. Comparison of Static Stability Derivatives Between Theory and Experiments for a Hemisphere-Cylinder	28
15. Comparison of Theoretical Results with and without Modification and Experimental Data	29
16. Comparison of Perturbation Theory with Nonlinear (Euler's Equations) Theory for a Hemisphere-Cylinder at $\alpha = 5$ deg and $M_\infty = 0.9$ and 1.2	31
17. Comparison of Theoretical Dynamic Stability Derivatives for a Parabolic Arc Nose	33
18. Comparison of Dynamic Stability Derivatives Between Theory and Experiments for a 2-Caliber Ogive-Nose-Cylinder	35
19. Comparison of Dynamic Stability Derivatives Between Theory and Experiments for a Hemisphere-Cylinder	36
APPENDIX	
A. DIFFERENCE FORM OF TERMS IN EQ. (18)	39
NOMENCLATURE	45

1.0 INTRODUCTION

Unsteady transonic flow over bodies has been treated with linear differential equations for high reduced frequencies with major interest in flutter analysis (Ref. 1). Since the frequency range of interest is the low frequency range, where the linearized equation breaks down, the nonlinear equation must be used. For slender bodies of revolution with a sharp nose, several investigators have developed approximate methods to solve the transonic small disturbance equation (Refs. 2 through 4). For blunt-nose bodies of revolution, these aforementioned methods are not applicable. In engineering applications, a method that can be applied to both blunt and pointed bodies of revolution is most desirable, and such a method is developed in this report.

The method to be described is based on the numerical method developed by South and Jameson (Ref. 5), who solved the steady full potential equation for axisymmetrical flow over blunt and pointed bodies of revolution at transonic speeds. Their method shows good agreement with other theoretical methods and experiments at steady state (Ref. 6). Thus, an extension of South and Jameson's scheme to calculate unsteady transonic flow has been pursued.

The unsteady motion under consideration is assumed to be a small amplitude harmonic oscillation; therefore, the flow may be divided into steady and unsteady components, with the latter as a perturbation of the former. The fundamental equations for the steady and unsteady parts were derived by using a body-normal coordinate system and are shown to be both elliptic and hyperbolic equations depending on the local steady flow Mach number. The numerical method of a rotated difference scheme developed in Ref. 5 was used in solving both the steady (computer program RAXBOD) and unsteady flow fields. Pulsatile and pitching oscillations were considered. Examples of the calculated results are given for both blunt and pointed bodies of revolution for quasi-steady and unsteady flow conditions.

2.0 ANALYSIS

2.1 BASIC EQUATIONS

The success of using a body-normal coordinate system with rotated difference scheme in predicting surface pressures of blunt and pointed bodies of revolution in steady transonic flow (Refs. 5 and 6) prompts one to use the same approach for the calculation of unsteady surface pressure. The unsteady potential equation for an irrotational compressible fluid (Ref. 7) is

$$\frac{1}{a^2} \cdot \frac{\partial^2 \phi}{\partial t^2} + \frac{2}{a^2} \vec{q} \cdot \frac{\partial \vec{q}}{\partial t} = \nabla^2 \phi - \frac{1}{a^2} \vec{q} \cdot [(\vec{q} \cdot \nabla) \vec{q}] \quad (1)$$

where ϕ is the velocity potential, \vec{q} is the velocity vector, a is the speed of sound, t is the time, and ∇ and ∇^2 are respectively the divergent and Laplace operators. If Eq. (1) is applied to a body-normal coordinate system (Fig. 1) for a body of revolution at zero incidence, one obtains

$$\begin{aligned} & \frac{1}{a^2} \cdot \frac{\partial^2 \phi}{\partial t^2} + \frac{2}{a^2} \left[\frac{U}{H} \cdot \frac{\partial^2 \phi}{\partial t \partial s} + V \frac{\partial^2 \phi}{\partial t \partial n} + \frac{W}{r} \frac{\partial^2 \phi}{\partial t \partial \psi} \right] \\ &= \left(1 - \frac{U^2}{a^2} \right) \frac{1}{H} \frac{\partial}{\partial s} \left(\frac{1}{H} \frac{\partial \phi}{\partial s} \right) - \left(1 - \frac{V^2}{a^2} \right) \frac{\partial^2 \phi}{\partial n^2} \\ &+ \left(1 - \frac{W^2}{a^2} \right) \frac{1}{r^2} \cdot \frac{\partial^2 \phi}{\partial \psi^2} - \frac{2}{a^2} \left(\frac{UV}{H} \cdot \frac{\partial^2 \phi}{\partial s \partial n} + \frac{VW}{r} \cdot \frac{\partial^2 \phi}{\partial n \partial \psi} \right. \\ &+ \left. \frac{WU}{Hr} \frac{\partial^2 \phi}{\partial s \partial \psi} \right) + \left(\frac{2UVK}{a^2 H} - \frac{\sin \theta}{r} \right) \frac{1}{H} \frac{\partial \phi}{\partial s} + \left[\frac{K}{H} \left(1 - \frac{U^2}{a^2} \right) \right. \\ &+ \left. \frac{\cos \theta}{r} \right] \frac{\partial \phi}{\partial n} + \left(\frac{V}{a} \cos \theta + \frac{U}{a} \sin \theta \right) \frac{W}{ar^2} \cdot \frac{\partial \phi}{\partial \psi} \end{aligned} \quad (2)$$

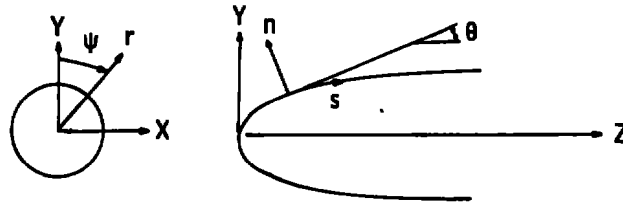
where

$$U = \cos \theta + \frac{1}{H} \cdot \frac{\partial \phi}{\partial s} \quad (3a)$$

$$V = -\sin \theta + \frac{\partial \phi}{\partial n} \quad (3b)$$

$$W = \frac{1}{r} \frac{\partial \phi}{\partial \psi} \quad (3c)$$

For flows about a body of revolution undergoing the small amplitude oscillation considered here, a $\cos \psi$ variation of the flow quantities in the ψ direction is assumed. It is also assumed that the solution can be expanded into a steady and an unsteady component (Ref. 4); i.e.,



$$H = 1 - \frac{d\theta}{ds} n$$

$$Z = \int \cos \theta \, ds - n \sin \theta$$

$$r = \int \sin \theta \, ds + n \cos \theta$$

Figure 1. Body-normal coordinate system.

$$\phi = \phi_0(s, n) + [\phi_1(s, n) \cos \psi e^{ikt}]_{R.P.} \quad (4a)$$

$$U = U_0 + (U_1 \cos \psi e^{ikt})_{R.P.} \quad (4b)$$

$$V = V_0 + (V_1 \cos \psi e^{ikt})_{R.P.} \quad (4c)$$

$$p = p_0 + (p_1 \cos \psi e^{ikt})_{R.P.} \quad (4d)$$

where k is the reduced frequency of the oscillation, R.P. signifies the real part of a complex quantity, and the subscripts 0 and 1 represent the quantity for steady and first-order perturbation flow, respectively. By substituting Eqs. (4a through d) into Eq. (2) and collecting terms of the same order, one obtains the zeroth-order equation for ϕ_0 as follows:

$$\begin{aligned} & \left(1 - \frac{U_0^2}{a_0^2}\right) \frac{1}{H} \frac{\partial}{\partial s} \left(\frac{1}{H} \frac{\partial \phi_0}{\partial s}\right) - \frac{2U_0 V_0}{a_0^2 H} \frac{\partial^2 \phi_0}{\partial s \partial n} + \left(1 - \frac{V_0^2}{a_0^2}\right) \frac{\partial^2 \phi_0}{\partial n^2} \\ & + \left[\frac{K}{H} \left(1 - \frac{U_0^2}{a_0^2}\right) + \frac{\cos \theta}{r}\right] \frac{\partial \phi_0}{\partial n} + \left[2 \frac{KU_0 V_0}{H a_0^2} + \frac{\sin \theta}{r}\right] \frac{1}{H} \frac{\partial \phi_0}{\partial s} = 0 \end{aligned} \quad (5)$$

$$U_0 = \cos \theta + \frac{1}{H} \frac{\partial \phi_0}{\partial s} \quad (6a)$$

$$V_0 = -\sin \theta + \frac{\partial \phi_0}{\partial n} \quad (6b)$$

The first-order equation for ϕ_1 is

$$\begin{aligned}
 & -k^2 \phi_1 + \frac{2ik}{a_o^2} \left[\frac{U_o}{H} \frac{\partial \phi_1}{\partial s} + V_o \frac{\partial \phi_1}{\partial n} \right] \\
 & = \left(1 - \frac{U_o^2}{a_o^2} \right) \frac{1}{H} \frac{\partial}{\partial s} \left(\frac{1}{H} \frac{\partial \phi_1}{\partial s} \right) + \left(1 - \frac{V_o^2}{a_o^2} \right) \frac{\partial^2 \phi_1}{\partial n^2} - \frac{C}{r^2} \phi_1 - \frac{2U_o V_o}{a_o^2 H} \cdot \frac{\partial^2 \phi_1}{\partial s \partial n} \\
 & \quad + \frac{A}{H} \frac{\partial \phi_1}{\partial s} + B \frac{\partial \phi_1}{\partial n}
 \end{aligned} \tag{7}$$

where

$$\begin{aligned}
 A = & \frac{2U_o V_o}{a_o^2 H} + \frac{\sin \theta}{r} - \frac{2U_o}{a_o^2 H} \frac{\partial}{\partial s} \left(\frac{1}{H} \frac{\partial \phi_o}{\partial s} \right) - 2 \left(\frac{\partial^2 \phi_o}{\partial s \partial n} \right) \frac{V_o}{a_o^2} \\
 & + \left(\frac{1}{H} \frac{\partial \phi_o}{\partial s} \right) \frac{2KV_o}{a_o^2 H} - \frac{K}{H} \frac{2U_o}{a_o^2} \left(\frac{\partial \phi_o}{\partial n} \right)
 \end{aligned} \tag{8a}$$

$$B = \frac{K}{H} \left(1 - \frac{U_o^2}{a_o^2} \right) + \frac{\cos \theta}{r} - \frac{2V_o}{a_o^2} \left(\frac{\partial^2 \phi_o}{\partial n^2} \right) - \frac{2U_o}{a_o^2} \left(\frac{\partial^2 \phi_o}{\partial s \partial n} \right) + \frac{2KU_o}{a_o^2 H} \left(\frac{1}{H} \frac{\partial \phi_o}{\partial s} \right) \tag{8b}$$

$$U_1 = \frac{1}{H} \frac{\partial \phi_1}{\partial s} \tag{9a}$$

$$V_1 = \frac{\partial \phi_1}{\partial n} \tag{9b}$$

The quantity C equals 0 or 1, depending on the type of flow under consideration. For axisymmetrical oscillatory flow such as the pulsatile oscillation, ϕ_1 is independent of ψ ; therefore, $\cos \psi$ should be replaced by unity in Eq. (4), and the term $(1/r^2 \phi_1)$ should be eliminated from Eq. (7); that is, $C = 0$. For a pitching oscillation, $C = 1$. Since Eq. (7) is a complex equation, ϕ_1 is a complex function and

$$\phi_1 = \phi_{IR}(s, n) + i\phi_{II}(s, n) \tag{10}$$

Consequently, U_1 , V_1 , and P_1 are all complex functions.

2.2 BOUNDARY CONDITIONS

The boundary condition is applied by requiring that the velocity vector be tangential to the surface, or

$$\frac{D\bar{B}}{Dt} = \frac{\partial \bar{B}}{\partial t} + U \frac{\partial \bar{B}}{\partial s} + V \frac{\partial \bar{B}}{\partial n} = 0 \quad (11)$$

and

$$\bar{B} = n - n_1(s, t) \quad (12)$$

Thus, the zeroth-order steady part boundary condition is

$$V_o = \frac{\partial \phi_o}{\partial n} - \sin \theta = 0 \quad (13)$$

and the first-order unsteady part boundary condition is

$$-\frac{\partial n_1}{\partial t} - \frac{U_o}{H} \frac{\partial n_1}{\partial s} + \frac{\partial \phi_1}{\partial n} = 0 \quad (14)$$

Also, at infinity ($n \rightarrow \infty$), the velocity potential is required to vanish; that is, $\phi_o \rightarrow 0$ and $\phi_1 \rightarrow 0$.

2.3 PRESSURE COEFFICIENTS

The pressure coefficients may be obtained by applying a perturbation approach to the unsteady Bernoulli equation, as follows:

$$\frac{p_o}{p_\infty} = 1 + \frac{\gamma-1}{2} M_\infty^2 \left[1 - U_o^2 - V_o^2 \right]^{\frac{\gamma}{\gamma-1}} \quad (15)$$

$$\frac{p_1}{p_\infty} = -\frac{\rho_o}{p_\infty} \left(\frac{\partial \phi_1}{\partial t} + \frac{U_o}{H} \frac{\partial \phi_1}{\partial s} + V_o \frac{\partial \phi_1}{\partial n} \right) \quad (16)$$

and

$$C_p = C_{p_o} + \Delta C_{p_1} \quad (17a)$$

$$\Delta C_{p_1} = C_{p_{1R}} + i \Delta C_{p_{1I}} \quad (17b)$$

where

$$C_{p_o} = \frac{p_o - p_\infty}{\frac{1}{2} \rho_\infty U_\infty^2} = \frac{2}{\gamma M_\infty^2} \left(\frac{p_o}{p_\infty} - 1 \right) \quad (17c)$$

$$\Delta C_{p_{1R}} = \frac{p_{1R} - p_\infty}{\frac{1}{2} \rho_\infty U_\infty^2} = \frac{2}{\gamma M_\infty^2} \left(\frac{p_{1R}}{p_\infty} - 1 \right) \quad (17d)$$

and

$$\Delta C_{p_{1I}} = \frac{p_{1I} - p_\infty}{\frac{1}{2} \rho_\infty U_\infty^2} = \frac{2}{\gamma M_\infty^2} \left(\frac{p_{1I}}{p_\infty} - 1 \right) \quad (17e)$$

3.0 COMPUTATIONAL SCHEME

The numerical method employed for the solution of the steady and unsteady flow fields is the same as that described in Ref. 5. In fact, the computer program RAXBOD developed by South at NASA Langley Research Center was used to solve the steady components, Eqs. (5) and (13). Figure 2 shows the transformation from the physical plane to the computational plane. The unsteady components are given by Eqs. (7) and (14). It should be noted that Eq. (7) retains the same transonic flow characteristics of a mixed-type, elliptic/hyperbolic differential equation, depending on whether the local steady flow is subsonic or supersonic. Hence, the scheme given in Ref. 5 was applied to solve Eqs. (7) and (14). However, since Eqs. (7) and (14) are linear, the finite difference equations obtained are a set of linear algebraic equations and can be solved by a direct matrix inversion instead of a relaxation method, which was used in the solution of the steady flow field (Ref. 5).

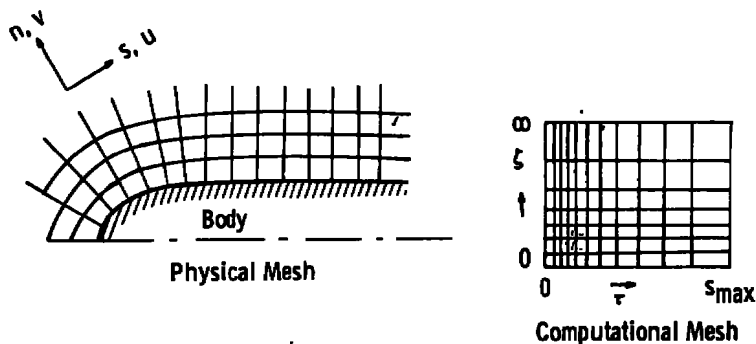


Figure 2. Transformation from physical to computational plane.

The details of the application of the rotated difference scheme and the relaxation method for solving the steady flow field may be found in Ref. 5 and will not be repeated herein. The implementation of the rotated difference scheme to the perturbed flow, Eq. (7), and the boundary condition, Eq. (14), as well as the system of algebraic equations, is given in this section.

3.1 DIFFERENCE EQUATIONS

To begin with, a simple case of a uniform cylindrical afterbody will be considered. Here, the sheared coordinates as described in Ref. 5 need not be used. When one applies the rotated difference scheme as described in Ref. 5, Eq. (7) is rewritten as follows:

$$\begin{aligned} \left(1 - \frac{q_o^2}{a_o^2}\right) \phi_{1R_{SS}} + \phi_{1R_{NN}} + C_4 \frac{1}{H} \cdot \frac{\partial \phi_{1R}}{\partial s} + C_5 \frac{\partial \phi_{1R}}{\partial n} \\ + C_6 \frac{1}{H} \frac{\partial \phi_{1I}}{\partial s} + C_7 \frac{\partial \phi_{1I}}{\partial n} + C_8 \phi_{1R} = 0 \end{aligned} \quad (18a)$$

$$\begin{aligned} \left(1 - \frac{q_o^2}{a_o^2}\right) \phi_{1I_{SS}} + \phi_{1I_{NN}} + C_4 \frac{1}{H} \frac{\partial \phi_{1I}}{\partial s} - C_5 \frac{\partial \phi_{1I}}{\partial n} \\ - C_6 \frac{1}{H} \frac{\partial \phi_{1R}}{\partial s} - C_7 \frac{\partial \phi_{1R}}{\partial n} + C_8 \phi_{1I} = 0 \end{aligned} \quad (18b)$$

where

$$\phi_{1R_{SS}} = \frac{1}{q_o^2} \left[\frac{U_o^2}{H} \frac{\partial}{\partial s} \left(\frac{1}{H} \frac{\partial \phi_{1R}}{\partial s} \right) - \frac{2U_o V_o}{H} \cdot \frac{\partial^2 \phi_{1R}}{\partial s \partial n} - V_o^2 \frac{\partial^2 \phi_{1R}}{\partial n^2} \right] \quad (19a)$$

$$\phi_{1R_{NN}} = \frac{1}{q_o^2} \left[\frac{U_o^2}{H} \frac{\partial}{\partial s} \left(\frac{1}{H} \frac{\partial \phi_{1R}}{\partial s} \right) - \frac{2U_o V_o}{H} \frac{\partial^2 \phi_{1R}}{\partial s \partial n} + V_o^2 \frac{\partial^2 \phi_{1R}}{\partial n^2} \right] \quad (19b)$$

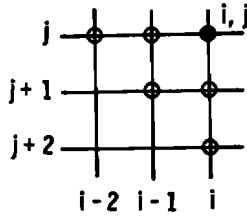
and

$$C_4 = A, \quad C_5 = B, \quad C_6 = \frac{2kU_o}{a_o^2}, \quad C_7 = \frac{2kV_o}{a_o^2}, \quad \text{and} \quad C_8 = \frac{k^2}{a_o^2} - \frac{C}{r^2} \quad (19c)$$

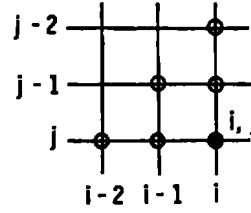
Similar equations may be written for $\phi_{1I_{SS}}$ and $\phi_{1I_{NN}}$. Now, the elliptic or hyperbolic nature of Eqs. (18a) and (18b) is determined by whether the local value of $(1 - q_o^2/a_o^2)$

is positive or negative, respectively. Thus, for all terms in Eq. (19a), if $(1 - q_0^2/a_0^2) > 0$, the central difference should be used, and if $(1 - q_0^2/a_0^2) < 0$, the upwind difference should be used. Furthermore, the upwind quadrant is determined by the sign of the local V_0 component as shown in Fig. 3. The corresponding different forms for terms in Eqs. (18a) and (18b) at the grid point (i, j) are expressed in Appendix A, and the final difference equations are given as follows:

For ϕ_{ss}
Supersonic Points:

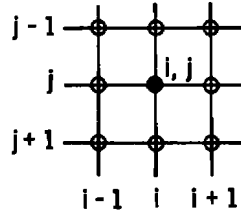


If $V > 0$



If $V \leq 0$

Subsonic Points:



Also for ϕ_{NN}

Figure 3. The neighboring points used in the difference scheme.

For a subsonic point

$$\begin{aligned}
 & (\beta_1 + a_1) \phi_{1R_{i-1,j-1}} + [(\beta_6 + a_6 - C_4') \phi_{1R} - C_6 \phi_{1I}]_{i-1,j} \\
 & + (\beta_7 + a_7) \phi_{1R_{i-1,j+1}} + [(\beta_2 + a_2 + C_5') \phi_{1R} + C_7' \phi_{1I}]_{i,j-1} \\
 & + (\beta_5 + a_5 + C_8) \phi_{1R_{i,j}} + [(\beta_8 + a_8 - C_5') \phi_{1R} - C_7' \phi_{1I}]_{i,j+1} \\
 & + (\beta_3 + a_3) \phi_{1R_{i+1,j-1}} - [(\beta_4 + a_4 + C_4') \phi_{1R} + C_6 \phi_{1I}]_{i+1,j} \\
 & + (\beta_9 - a_9) \phi_{1R_{i+1,j+1}} = 0
 \end{aligned} \tag{20}$$

For a supersonic point and $V > 0$

$$\begin{aligned}
 & \gamma_1 \phi_{1R_{i-2,j}} + a_1 \phi_{1R_{i-1,j-1}} + [(a_6 + \gamma_2 - C_4') \phi_{1R} - C_6' \phi_{1I}]_{i-1,j} \\
 & + (a_7 + \gamma_4) \phi_{1R_{i-1,j+1}} + [(a_2 + C_3') \phi_{1R} + C_7' \phi_{1I}]_{i,j-1} \\
 & + (a_5 + \gamma_3 + C_8) \phi_{1R_{i,j}} + [(a_8 + \gamma_5 - C_5') \phi_{1R} - C_7' \phi_{1I}]_{i,j+1} \\
 & + \gamma_6 \phi_{1R_{i,j+2}} + [(a_4 + C_4') \phi_{1R} - C_6' \phi_{1I}]_{i+1,j} \\
 & + a_9 \phi_{1R_{i+1,j+1}} = 0
 \end{aligned} \tag{21}$$

For a supersonic point and $V \leq 0$

$$\begin{aligned}
 & \gamma_1 \phi_{1R_{i-2,j}} + (a_1 - \gamma_4) \phi_{1R_{i-1,j-1}} + [(a_6 + \gamma_2 - C_4') \phi_{1R} \\
 & - C_6' \phi_{1I}]_{i-1,j} - a_7 \phi_{1R_{i-1,j-1}} + \gamma_6' \phi_{1R_{i,j-2}} \\
 & + [(a_2 - \gamma_5 + C_5' + a_3) \phi_{1R} + C_7' \phi_{1I}]_{i,j-1} \\
 & + [(a_5 - \gamma_3 + C_8 + a_4 + C_4') \phi_{1R} - C_6' \phi_{1I}]_{i,j} \\
 & + [(a_8 - C_5' + a_9) - C_7' \phi_{1I}]_{i,j+1} = 0
 \end{aligned} \tag{22}$$

Similar equations can be written for ϕ_{1I} by switching ϕ_{1R} and ϕ_{1I} and changing the sign for C_6' and C_7' in Eqs. (20) through (22); thus these equations will not be repeated herein.

Special treatment is required for the perturbed flow ϕ_1 along the axis, as was the case for the steady part ϕ_0 . For axisymmetric unsteady flow such as a pulsatile oscillation, for example, $s \rightarrow 0$,

$$U_0 \rightarrow 0, \quad r \rightarrow H_0 s \rightarrow 0, \quad \theta \rightarrow \frac{\pi}{2}, \quad \frac{\partial \phi_0}{\partial s} \rightarrow 0 \tag{23a}$$

and

$$U_1 \rightarrow 0 \tag{23b}$$

Equation (18) reduces to

$$\frac{1}{H_o^2} \left(\frac{\partial^2 \phi_{1R}}{\partial s^2} \right) + \left(1 - \frac{V_o^2}{a_o^2} \right) \frac{\partial^2 \phi_{1R}}{\partial n^2} + B \frac{\partial \phi_{1R}}{\partial n} + \frac{2kV_o}{a_o^2} \frac{\partial \phi_{1I}}{\partial n} + \left(\frac{k^2}{a_o^2} \right) \phi_{1R} = 0 \quad (24a)$$

$$\frac{1}{H_o^2} \left(\frac{\partial^2 \phi_{1I}}{\partial s^2} \right) + \left(1 - \frac{V_o^2}{a_o^2} \right) \frac{\partial^2 \phi_{1I}}{\partial n^2} + B \frac{\partial \phi_{1I}}{\partial n} - \frac{2kV_o}{a_o^2} \frac{\partial \phi_{1R}}{\partial n} - \left(\frac{k^2}{a_o^2} \right) \phi_{1I} = 0 \quad (24b)$$

where

$$B = \frac{2k}{H_o} - \frac{2V_o}{a_o^2} \left(\frac{\partial^2 \phi_o}{\partial n^2} \right)$$

Equation (24) should be used along the axis, or $i = 1$. If the perturbed flow is not axisymmetric, as in the case of pitching or heaving oscillations, then because of the assumption that ϕ_1 is antisymmetrical with respect to ψ (i.e., $\phi_1 \sim \cos \psi$), ϕ_{1R} and ϕ_{1I} must be zero along the axis.

Again, the upwind difference should be applied to the second term in Eqs. (24) when $(1 - V_o^2/a_o^2) < 0$ and the central difference should be used when $(1 - V_o^2/a_o^2) > 0$. For other terms, the central difference should be used. Hence, at each grid point, two algebraic equations are obtained for ϕ_{1R} and ϕ_{1I} , and these two equations are coupled through the terms with coefficient C'_6 and C'_7 . For points involving boundaries, such as the body surface, the axis of symmetry, and infinity, the proper boundary condition should be imposed (to be discussed later). Hence, the total number of algebraic equations to be solved simultaneously will be $2 \times (I - 1) \times (J - 1)$, where I and J are the maximum grid index along the s and n directions, respectively.

3.2 BOUNDARY CONDITIONS

The surface boundary condition, Eq. (14), may be rewritten as follows:

$$\frac{\partial \phi_{1R}}{\partial n} = \frac{U_o}{H} \cdot \frac{\partial n_1}{\partial s} \quad (25a)$$

$$\frac{\partial \phi_{1I}}{\partial n} = k n_1 \quad (25b)$$

where n_1 is given by the motion of the body and will be described later. In difference form, Eqs. (25a) and (25b) become

$$\phi_{1R_{i,J+1}} = -\frac{2\Delta\zeta}{g_1} \left(\frac{U_o}{H} \frac{\partial n_1}{\partial s} \right) + \phi_{1R_{i,J-1}} \quad (26a)$$

$$\phi_{1I_{i,J+1}} = -\frac{2\Delta\zeta}{g_1} (kn_1) + \phi_{1I_{i,J-1}} \quad (26b)$$

Equations (26a) and (26b) will be used to replace all terms at J+1.

The expressions for n_1 for three oscillatory motions which have engineering applications are now described.

(1) Pulsatile oscillation with the amplitude proportional to the local radius:

$$n_1 = \delta_o (r \cos \theta) \quad (27a)$$

$$\frac{\partial n_1}{\partial s} = \delta_o (K r \sin \theta + H \cos \theta \sin \theta) \quad (27b)$$

(2) Pitching oscillation with amplitude τ_o :

$$n_1 = \tau_o (d_t - Z) \cos \theta \quad (28a)$$

$$\frac{\partial n_1}{\partial s} = \tau_o (d_t - Z) K \sin \theta - \cos^2 \theta \quad (28b)$$

where d_t is the pitch center.

(3) Heaving oscillation with amplitude h_o :

$$n_1 = h_o \cos \theta \quad (29a)$$

$$\frac{\partial n_1}{\partial s} = h_o K \sin \theta \quad (29b)$$

The boundary condition at infinity is $\phi_{1R} = \phi_{1I} = 0$ or all values of ϕ_{1R} and ϕ_{1I} at $j = 1$ are zero.

The boundary condition at the axis for axisymmetric flow becomes

$$\phi_{1R_{i+1,j}} = \phi_{1R_{i-1,j}} \quad (30a)$$

$$\phi_{1I_{i+1,j}} = \phi_{1I_{i-1,j}} \quad (30b)$$

For nonaxisymmetric flow, one obtains

$$\phi_{1R_{i+1,j}} = \phi_{1R_{i-1,j}} \quad \text{and} \quad \phi_{1R_{i,j}} = 0 \quad (31a)$$

$$\phi_{1I_{i+1,j}} = -\phi_{1I_{i-1,j}} \quad \text{and} \quad \phi_{1I_{i,j}} = 0 \quad (31b)$$

because of the $\cos \psi$ variation of the flow in the crossflow plane. The set of linear algebraic equations was solved by the method of factorization.

4.0 RESULTS AND DISCUSSION

4.1 GENERAL REMARKS

A computer program to solve for the perturbed flow field was coded for an IBM 370-165 computer. The computational procedure was first to compute the steady flow field using the computer program RAXBOD. The values of ϕ_0 in each node and other required information were stored; then all the coefficients for the algebraic equation and the perturbed boundary conditions for a given oscillatory motion were computed. Finally, a simultaneous solution of the algebraic equations gave the values of ϕ_{1R} and ϕ_{1I} at every nodal point. All perturbed flow quantities could now be obtained by differencing the ϕ_0 , ϕ_{1R} , and ϕ_{1I} values.

Regarding the selection of the nodal distribution to give good resolution, two sets of 97×33 and 97×97 were frequently used for the steady part calculation. For the perturbed unsteady part, four nodal distributions were tried (i.e., 25×9 , 49×17 , 97×17 , and 97×33). The results obtained from 25×9 were not satisfactory in many cases, particularly at a supersonic free-stream velocity. The results obtained from the 49×17 , 97×17 , and 97×33 matrices have good agreement in many cases. The required computer time is about 1-1/2 min. for 49×17 , 4 min. for 97×17 , and 30 min. for 97×33 . It was decided that the nodal distribution of 97×17 was sufficiently good from the standpoints both of accuracy and economy. Therefore, most results presented in this report are obtained using 97×17 nodes.

4.2 PULSATILE OSCILLATION

A body of revolution undergoing oscillatory, pulsatile motion of the surface is a fundamental axisymmetric, unsteady motion. For the perturbation method developed in this report, the pulsatile oscillation can also provide a direct comparison between the quasi-steady solution of the linear perturbed equation (Eq. (7)) and the steady-state solution of the nonlinear equation (identical to Eq. (5)) for the same body geometry. The case

of a hemisphere-cylinder was chosen for comparison. The magnitude of the pulsatile oscillation is assumed to be proportional to $0.1 r$, where r is the local radius of the body. As shown in Fig. 4, the expanded ($R_t = 1.1$) and the shrunk ($R_t = 0.9$) bodies are an ellipse-cylinder with nose axis ratios of 1.1 and 0.9, respectively. The steady-state solution for the surface pressure shown in solid curves in Figs. 4 ($M_\infty = 0.6$) and 5 ($M_\infty = 1.2$) for the ellipse-cylinders was obtained directly from the computer program RAXBOD. The quasi-steady solution for the same ellipse-cylinders can be obtained by adding (for $R_t = 1.1$) or subtracting (for $R_t = 0.9$) the perturbed pressure from the mean steady-state surface pressure for a hemisphere-cylinder ($R_t = 1.0$). The quasi-steady solutions, as shown by broken curves in Figs. 4 and 5, are seen to agree well with the steady-state solution.

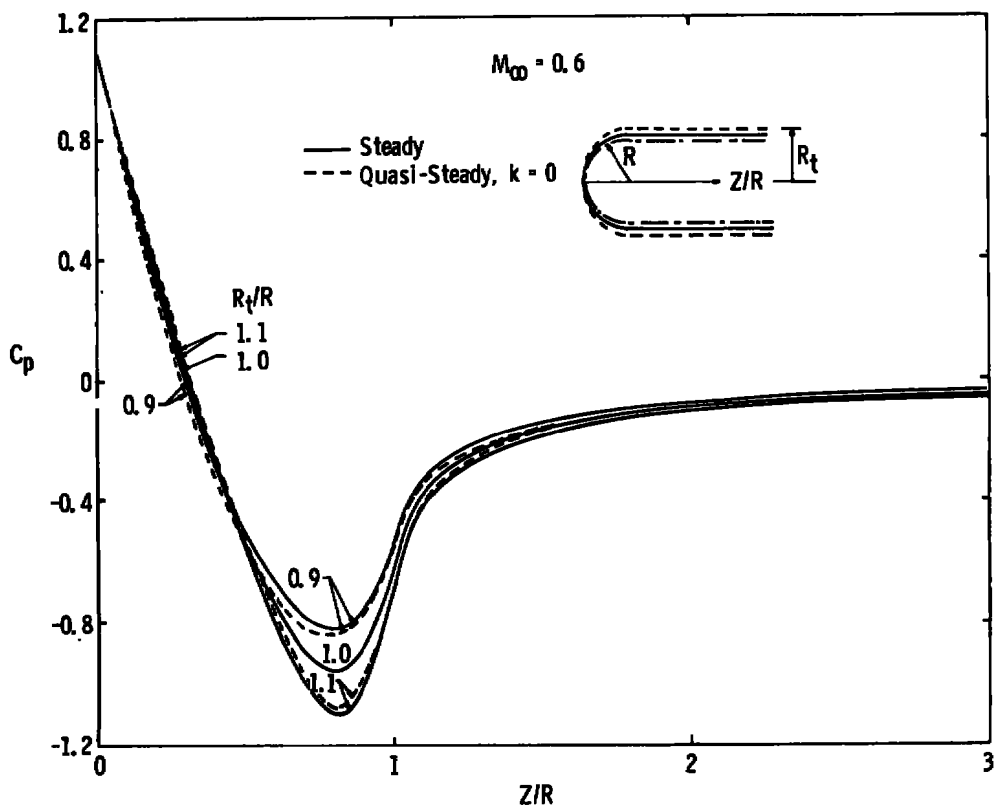


Figure 4. Quasi-steady surface pressure perturbation for hemisphere-cylinder at $M_\infty = 0.6$.

4.3 PITCHING OSCILLATION

Calculations for a pitching oscillation were performed for five body configurations: (a) 4-caliber ogive-nose-cylinder with $l/R = 20$; (b) 2-caliber ogive-nose-cylinder with l/R

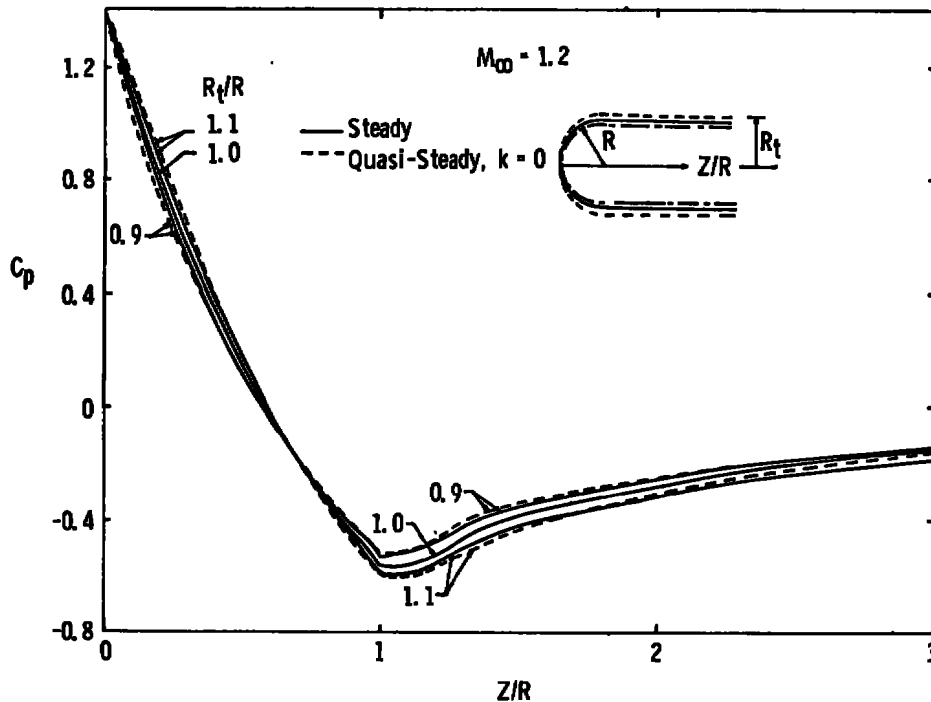


Figure 5. Quasi-steady surface pressure perturbation for hemisphere-cylinder at $M_\infty = 1.2$.

= 14; (c) 2:1 ellipse-nose-cylinder with $\ell/R = 20$; (d) hemisphere-cylinder with $\ell/R = 14$; and (e) parabolic arc nose with $\ell/R = 5$. The quasi-steady ($k = 0$) solutions for the surface pressure will be compared to steady experimental data for configurations a, c, and d at zero and nonzero incidence. The quasi-steady aerodynamic coefficients and the nonsteady damping-in-pitch coefficients will be compared to experimental data and available theory for configurations b, d, and e.

4.3.1 Quasi-Steady Perturbation Pressure

4.3.1.1 The 4-Caliber Ogive-Nose-Cylinder

In Fig. 6, the steady-state solution for surface pressure ($M_\infty = 0.8$ to 1.1) for the 4-caliber-ogive-nose-cylinder compares satisfactorily with the experimental data (Ref. 8) at zero incidence. Thus, the steady-part solution, which was used as the input for the unsteady part calculation, is valid. The quasi-steady solution for the perturbed surface pressure is shown in Fig. 7 for the leeward plane of symmetry (all discussion in this report is referred to the leeward plane of symmetry). Since the perturbed flow field is linear with respect to the incidence, the magnitude of $\overline{\Delta C_p}/a$ is plotted. In Ref. 8, two

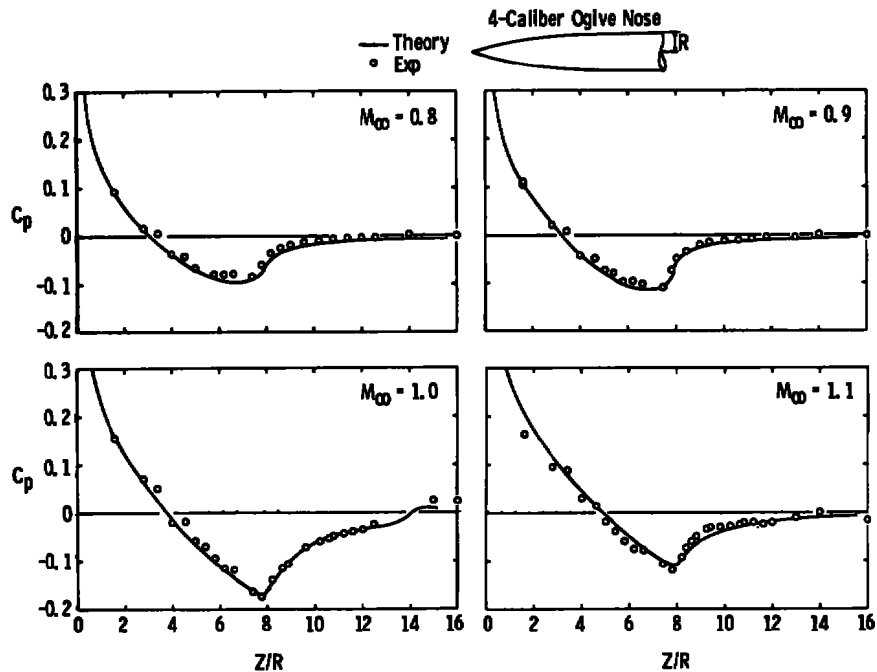


Figure 6. Comparison of steady-state surface pressure between theory and experiments for a 4-caliber ogive-nose-cylinder.

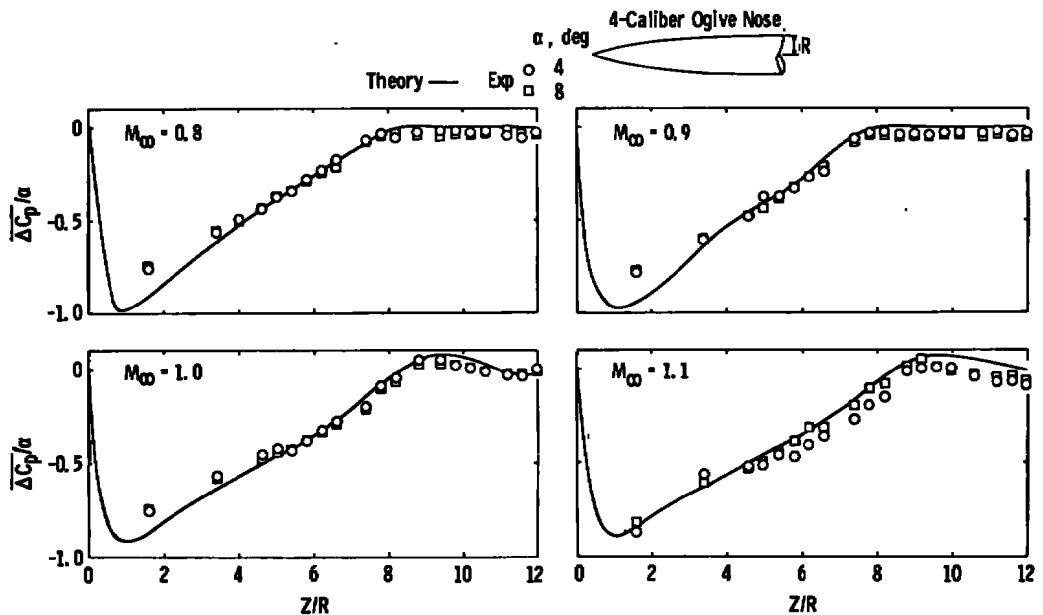


Figure 7. Comparison of quasi-steady perturbed surface pressure between theory and experiments for a 4-caliber ogive-nose-cylinder.

sets of experimental data were obtained for $\alpha = \pm 4$ and ± 8 deg. To obtain the average perturbed pressure slope for comparison, the following formula was used.:

$$\frac{\overline{\Delta C_p}}{\alpha} = \frac{(C_{p\alpha} - C_{p-\alpha})}{2\alpha} \quad (32)$$

Figure 7 shows that the agreement between theory and experiment is excellent. That the data for $\alpha = \pm 8$ and ± 4 deg agree well, except at $M_\infty = 1.1$, indicates the linearity of the perturbed flow up to 8 deg.

4.3.1.2 The 2:1 Ellipse-Nose-Cylinder

In Fig. 8, the steady-state solutions for surface pressure ($M_\infty = 0.6$ to 1.2) for the 2:1 ellipse-nose-cylinder again compare satisfactorily with the experimental data (Ref. 8)

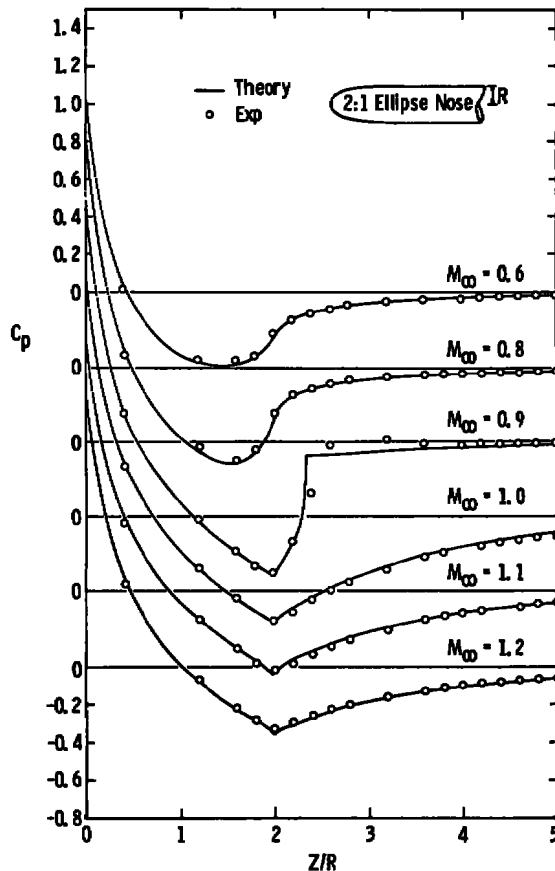
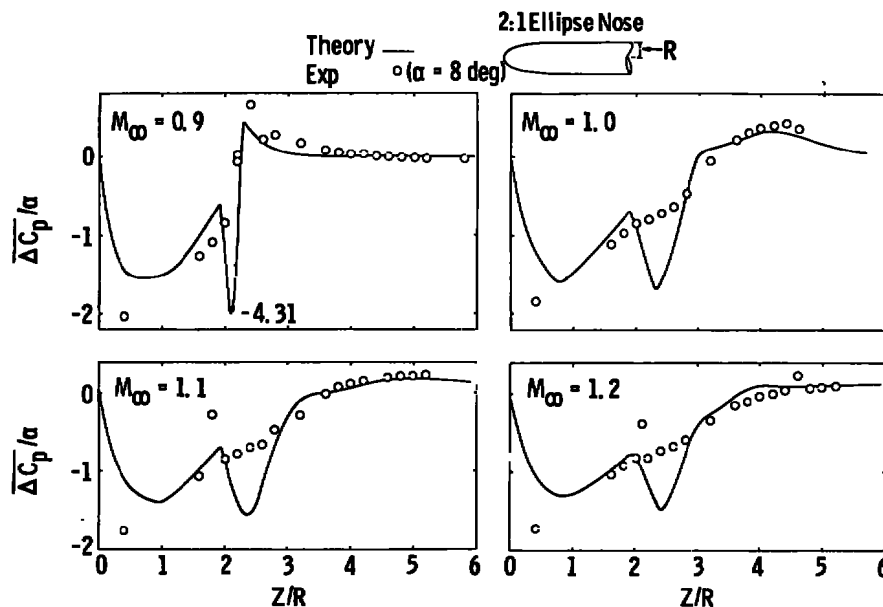


Figure 8. Comparison of steady-state surface pressure between theory and experiments for a 2:1 ellipse-nose-cylinder.

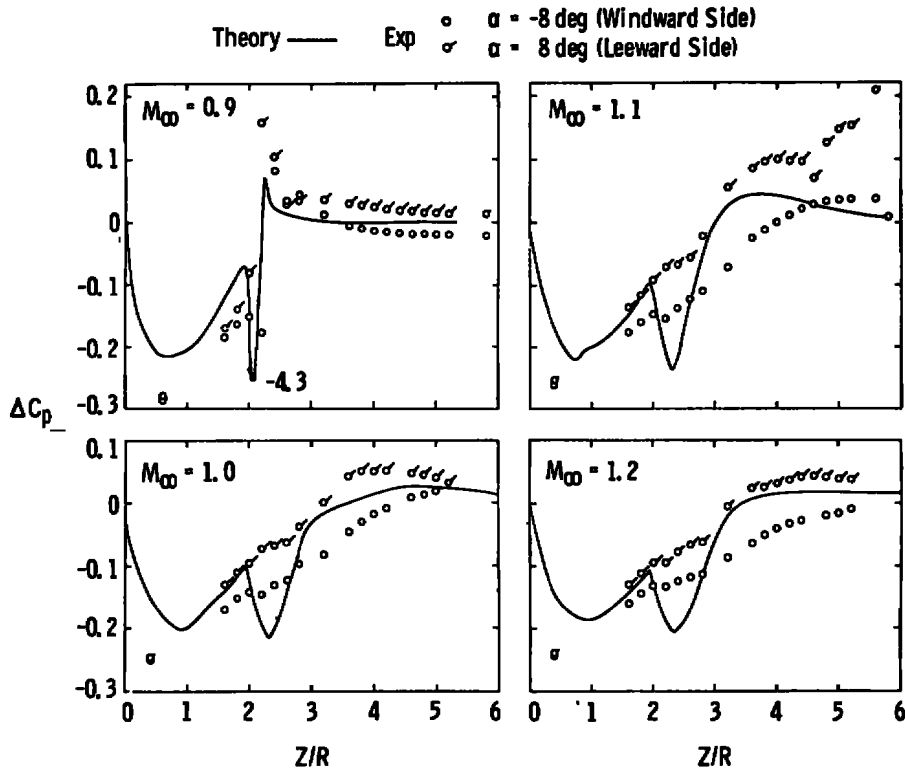
at zero incidence. At incidence, the experimental data were obtained for $M_\infty = 0.9$ to 1.2 and $\alpha = \pm 8$ deg only. The comparison between the quasi-steady theory and experiments for the average perturbed surface pressure is given in Fig. 9a. The agreement is generally good. However, the theoretical data show a spike and dip for $M_\infty = 0.9$ and a hump for $M_\infty \geq 1.0$ aft of the juncture of the ellipse and the cylinder. These phenomena are not shown by the experimental data. The cause may be attributed to the discontinuity in the curvature of the body geometry in the inviscid calculation of the perturbed flow field. In order to show the effect of curvature discontinuity, plots of the experimental



a. Average perturbed surface pressure

Figure 9. Comparison of quasi-steady perturbed surface pressure between theory and experiments for a 2:1 ellipse-nose-cylinder.

leeward side perturbation pressure ($C_{p_{\alpha=8^\circ}} - C_{p_{\alpha=0^\circ}}$) and windward side perturbation pressure ($C_{p_{\alpha=0^\circ}} - C_{p_{\alpha=8^\circ}}$) are presented in Fig. 9b. Interestingly enough, the experimental data for the windward side do show the expected type of peak and dip for $M_\infty = 0.9$ and the expected hump for $M_\infty \geq 1.0$ approximately in the locations given by the theory, but to a far lesser degree than indicated. The experimental data in the leeward side behave in a significantly different manner from those of the windward side in $2 < z/R < 2.5$ for M_∞ from 0.9 to 1.1, indicating the effect of viscosity and hence the deviation from the assumption of a $\cos \psi$ flow field at $\alpha = 8$ deg.



b. Windward and leeward side perturbed surface pressure
 Figure 9. Concluded.

4.3.1.3 The Hemisphere-Cylinder

The third configuration used for surface pressure comparison is a hemisphere-cylinder. A good agreement in the surface pressure between theory and experiment at zero incidence when there is no flow separation has been shown in Ref. 9, but flow separation does occur at $M_\infty = 0.7$ to 0.9 at zero incidence. To evaluate the quasi-steady theory at incidence, the Ref. 9 experimental data for hemisphere-cylinders at $\alpha = \pm 5$ deg were used. (In Ref. 9, $\phi = 0$ and 180 deg, which corresponds to $\alpha = 5$ and -5 deg, used herein.) In Fig. 10, the leeward and windward side perturbation pressures are compared between theory and experiment for $M_\infty = 0.6, 0.7, 0.8, 0.9, 1.0$, and 1.2 . In Fig. 11, the shadowgraphs of the flow field at $\alpha = 5$ deg are shown. At $M_\infty = 0.6$, Fig. 11 shows that the flow is attached except for a possible minor separation near the juncture of the hemisphere and the cylinder. This separation is also indicated by the experimental data of the perturbation pressure on the leeward and windward sides. The theory seems to slightly overpredict the perturbation pressure. For $M_\infty = 0.7$ to 0.9 , Fig. 11 shows that the leeward flow separates. On the windward side, a small shock system is indicated for $M_\infty = 0.7$; for $M_\infty = 0.8$, the shock system resembles the case of $\alpha = 0$, which indicates the existence

of a separation bubble (see Ref. 9). For $M_\infty = 0.9$, an embedded normal shock is shown. For the described flow field, one would not expect good agreement between the theory and the experiments because of viscous effects. As shown in Fig. 10, the agreement is

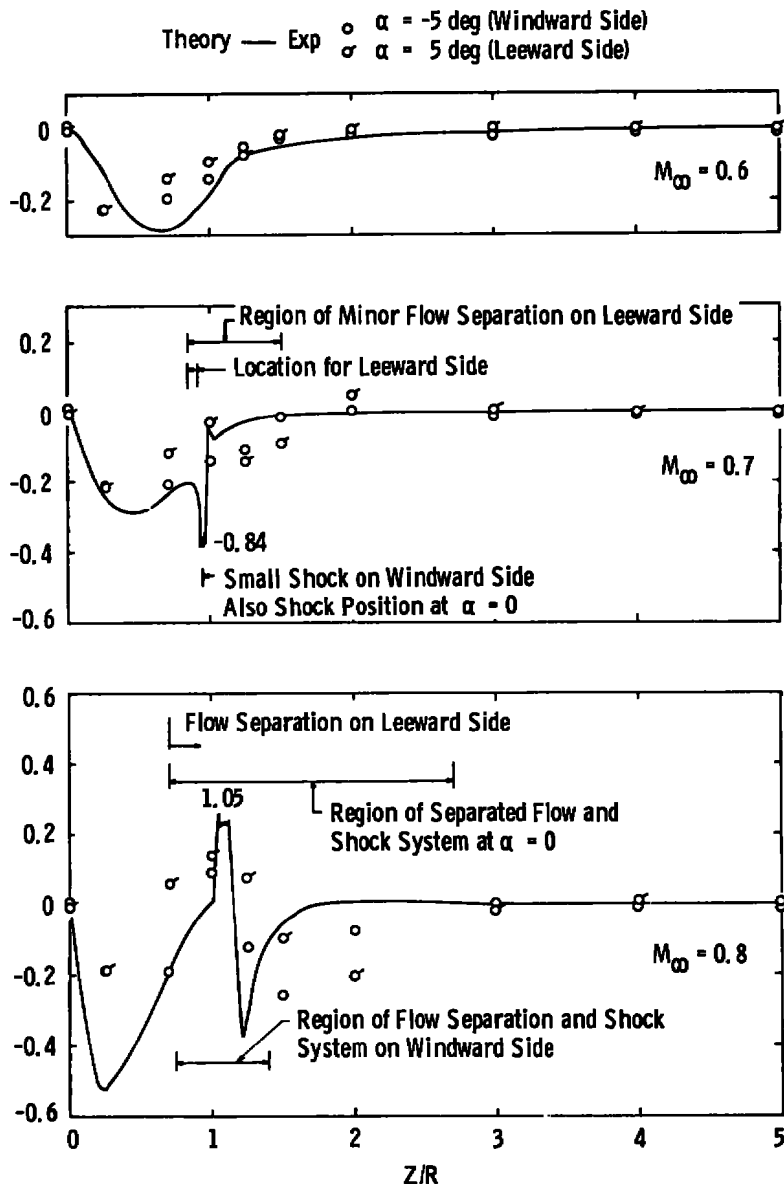


Figure 10. Comparison of quasi-steady perturbed surface pressure between theory and experiments for a hemisphere-cylinder.

poor for these cases just discussed. It is noted that there are spikes in the theoretical curves for $M_\infty = 0.7$ to 0.9 at the region near the zero incidence shock location. The calculated values at the spikes are unrealistic because of the large gradients in the flow quantities near the shock (see Section 4.3.4 for modification). For $M_\infty = 1.0$ and 1.2 , Fig. 11 shows that the flow is again well attached, which is also indicated by the experimental data shown in Fig. 10. Thus, for $M_\infty = 1.0$ and above, the comparison between theory and experiments is good except for the hump resulting from the curvature discontinuity aft of the junction of the hemisphere and the cylinder, where the theory shows a larger value again.

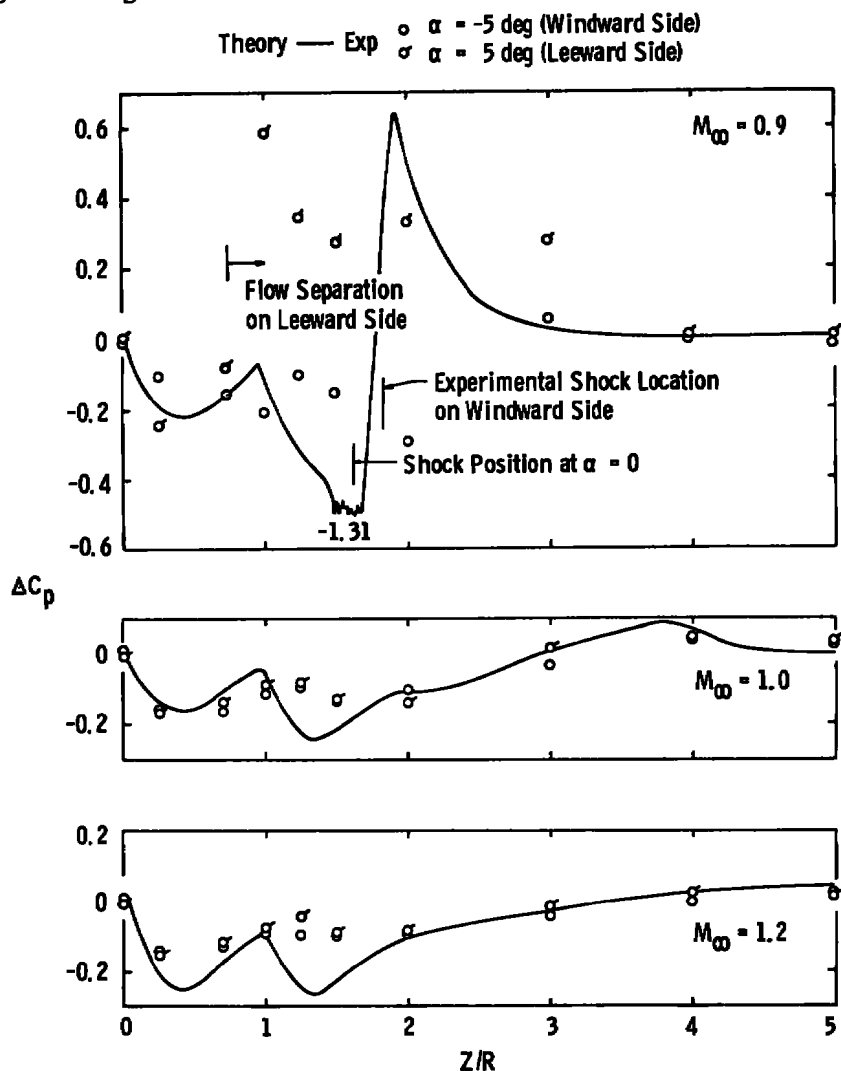
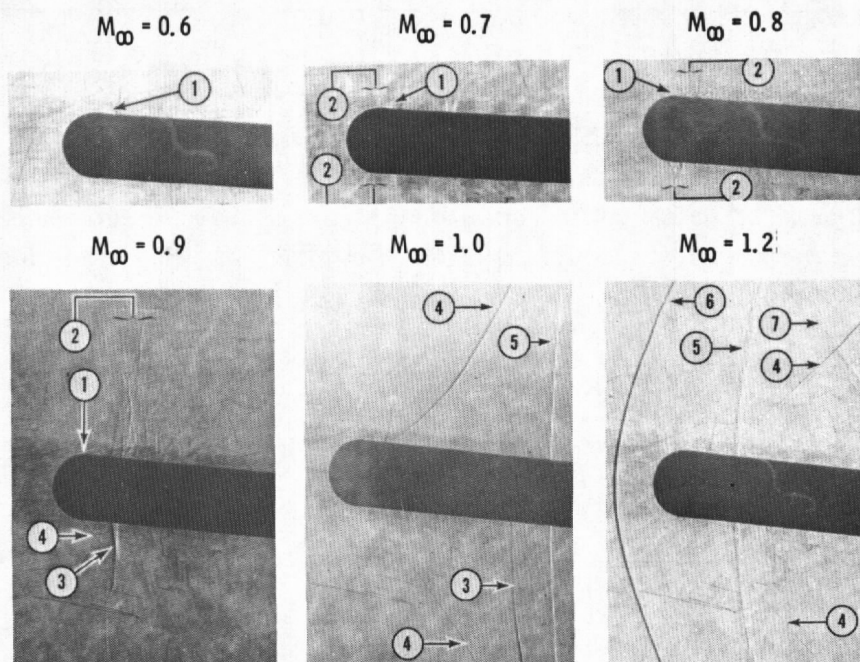


Figure 10. Concluded.



- ① Flow Separation
- ② Embedded Shock System
- ③ Embedded Normal Shock
- ④ Recompression Shock
- ⑤ Intersection of Shock and Tunnel Side Walls
- ⑥ Bow Shock
- ⑦ Disturbances Reflected from Wall Due to Bow Shock

Figure 11. Shadowgraphs of hemisphere-cylinder at 5 deg.

4.3.2 Shock Excursion at Incidence

The surface pressure obtained by the perturbation theory and the experimental data are presented in Fig. 12 for the ellipse-cylinder at $M_\infty = 0.9$ and $\alpha = 0$ and ± 8 deg (no serious flow separation occurs on the leeward side of this case). At $\alpha = 0$ the shock occurs at approximately $Z/R = 2.3$, where the pressure increases sharply. It is noted that the experimental data for $\alpha = \pm 8$ deg cross over the data for $\alpha = 0$. This is an indication of the moving of the shock as the body pitches to an angle. For example, if the body is at positive incidence (leeward side), the shock will move forward from 0 to 1 as shown in the sketch in Fig. 12. The surface pressure in between the points 0 and 1 will increase due to the forward moving of the shock, whereas upstream of 1 the pressure will decrease

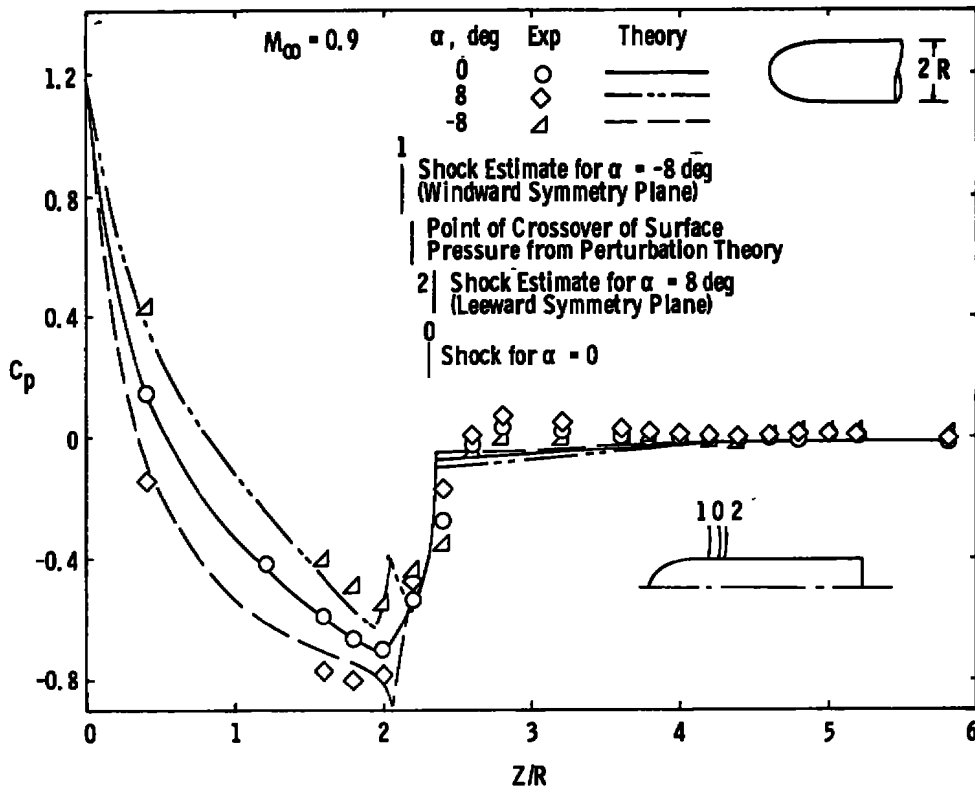


Figure 12. Comparison of surface pressure between theory and experiments for a 2:1 ellipse-nose-cylinder at incidence and $M_\infty = 0.9$.

due to the incidence. For negative incidence (windward side) the shock moves to 2; then the pressure upstream of 0 increases, but the pressure in between 0 and 2 should decrease due to the aft movement of the shock from 0 to 2. Thus, when the data at incidence cross over at zero incidence, this point of crossover may be interpreted as the location of the shock at incidence. The excursion of the shock as read by this method is shown in Fig. 12. Since the distance between points 1 and 2 is about $0.2R$ and covers a total incidence of 16° , the shock excursion is relatively small for bodies of revolution as compared to a 2-D airfoil for which a 10-percent chord length excursion over a few degrees of incidence is common. In addition, the theoretical result shows a point of crossover in the surface pressure near the middle of points 1 and 2 and has the same trend as shown by the experimental data. Therefore, the presumed fixed shock location in the development of the perturbation theory for bodies of revolution is not a serious deficiency when the shock is not too strong. If, however, the normal shock is strong (for increasing bluntness of the nose), as for the case of a hemisphere-cylinder, the flow in the leeward side is generally separated, and the inviscid calculation is invalidated. For the windward

side, however, the shock excursion is not large (about $0.2R$), as shown in Fig. 10 for $M_\infty = 0.9$.

4.3.3 Quasi-Steady Aerodynamic Coefficients

The integrated aerodynamic coefficients for the 2-caliber ogive-nose-cylinder and the hemisphere-cylinder are shown in Figs. 13 and 14, respectively. The experimental force data were obtained from Refs. 9 and 10. The theoretical value of $C_{A,F}$ is the same as at $\alpha = 0$ and is generally lower than the experiments. However, experimental force data

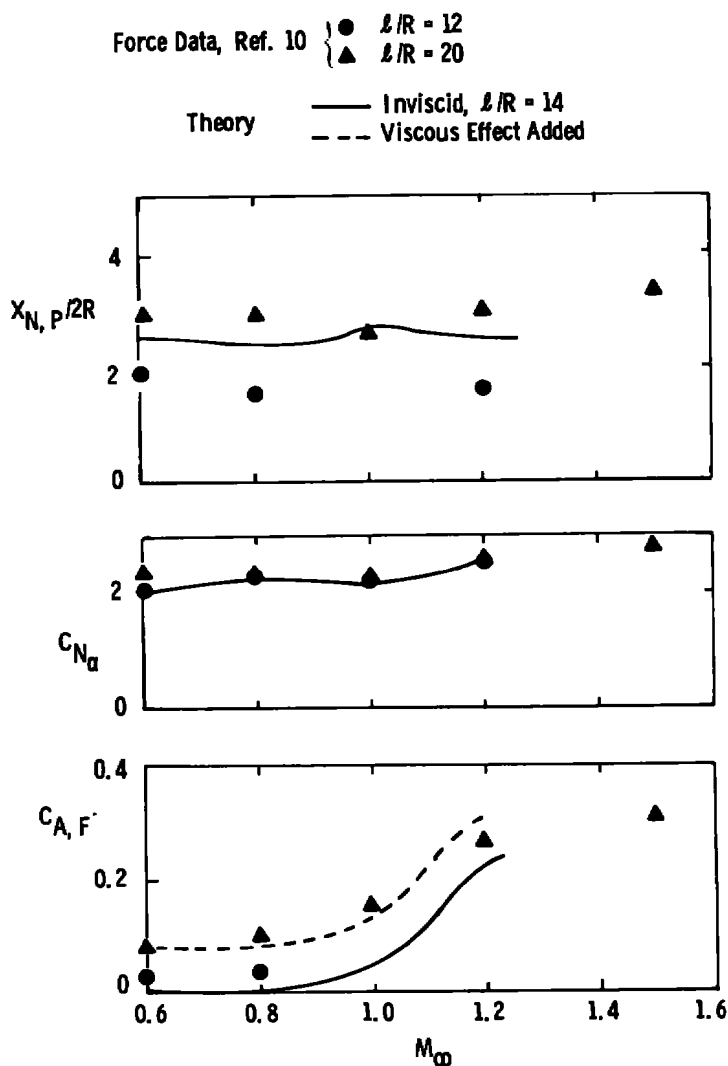


Figure 13. Comparison of static stability derivatives between theory and experiments for a 2-caliber ogive-nose-cylinder.

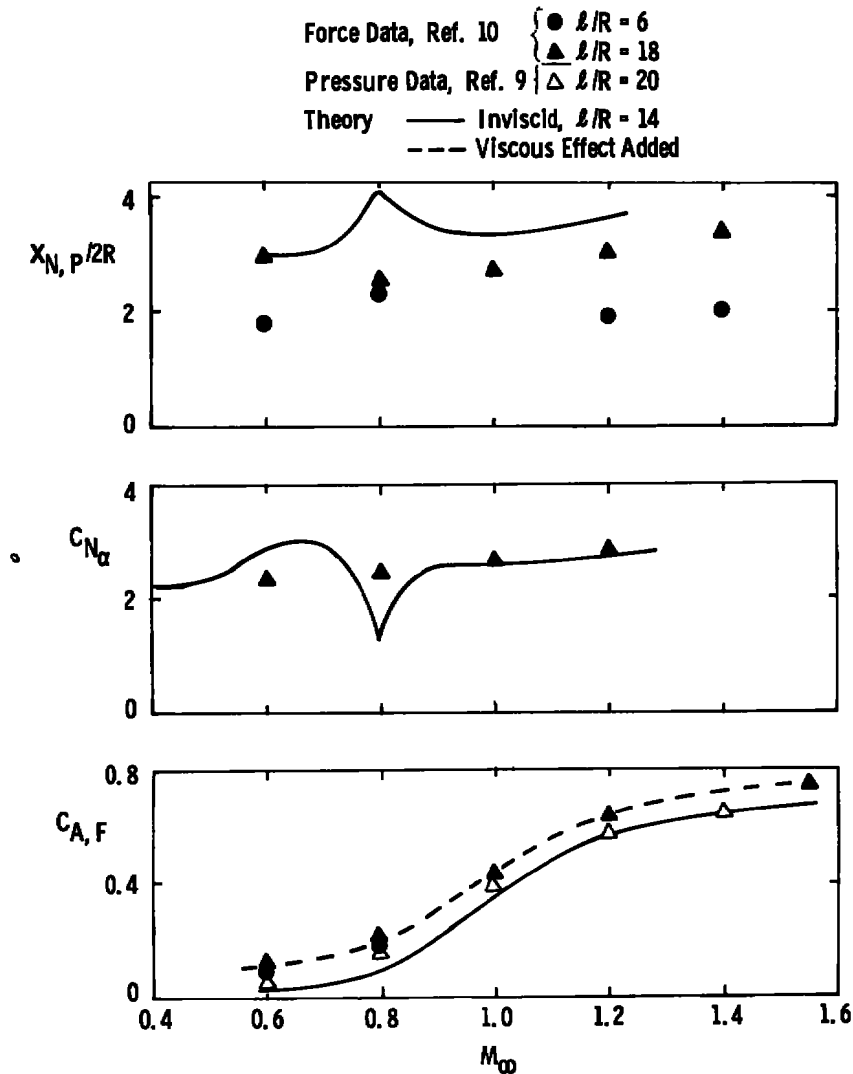


Figure 14. Comparison of static stability derivatives between theory and experiments for a hemisphere-cylinder.

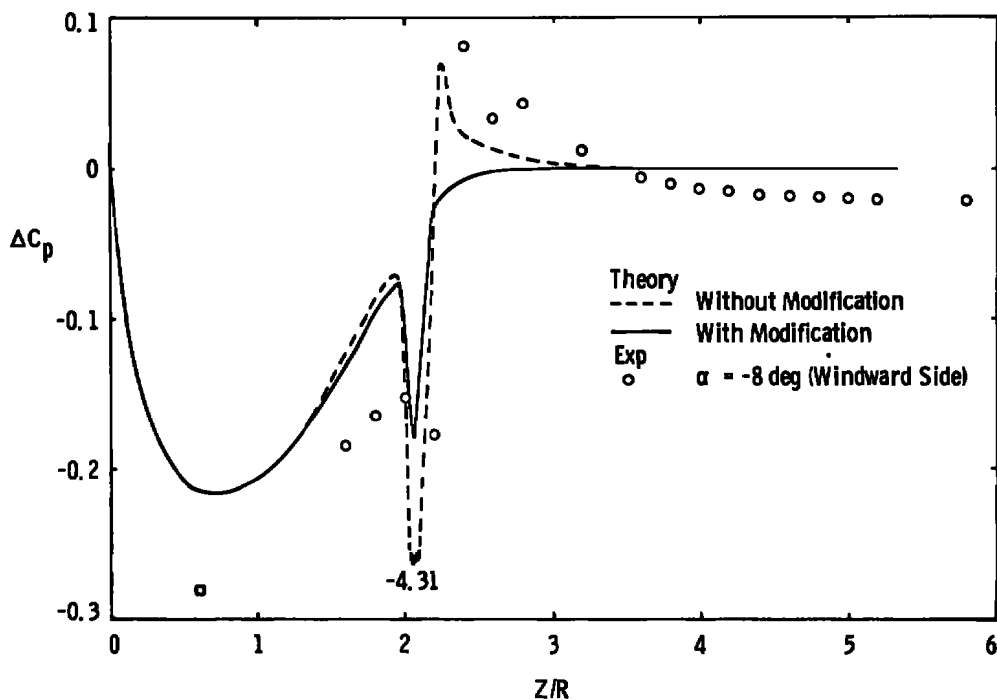
for the shorter body and the integration of surface pressure measurements for the hemisphere-cylinder (Fig. 14) do show better agreement with the theory. This indicates that the difference is due to the skin friction, which was not accounted for in the theory. When the viscous effect is added, using a skin friction corresponding to the experimental Reynolds number for the long body only, the agreement between theory and experiments for $C_{A, F}$ is excellent. The C_{N_α} value is nearly independent of the body length and is shown to be in good agreement with the theory for the ogive-cylinder. For the hemisphere-cylinder, the hump and dip in the C_{N_α} data, given by the theory as between

Mach numbers from 0.6 to 0.9, were not shown by the experimental data; but for $M_\infty \geq 0.9$ the agreement is again good. The aerodynamic moment center (neutral point) measured from the body midpoint (positive forward) is compared between theory and experiments in Figs. 13 and 14; the agreements are only fairly good.

4.3.4 Modification at the Region of Embedded Shock

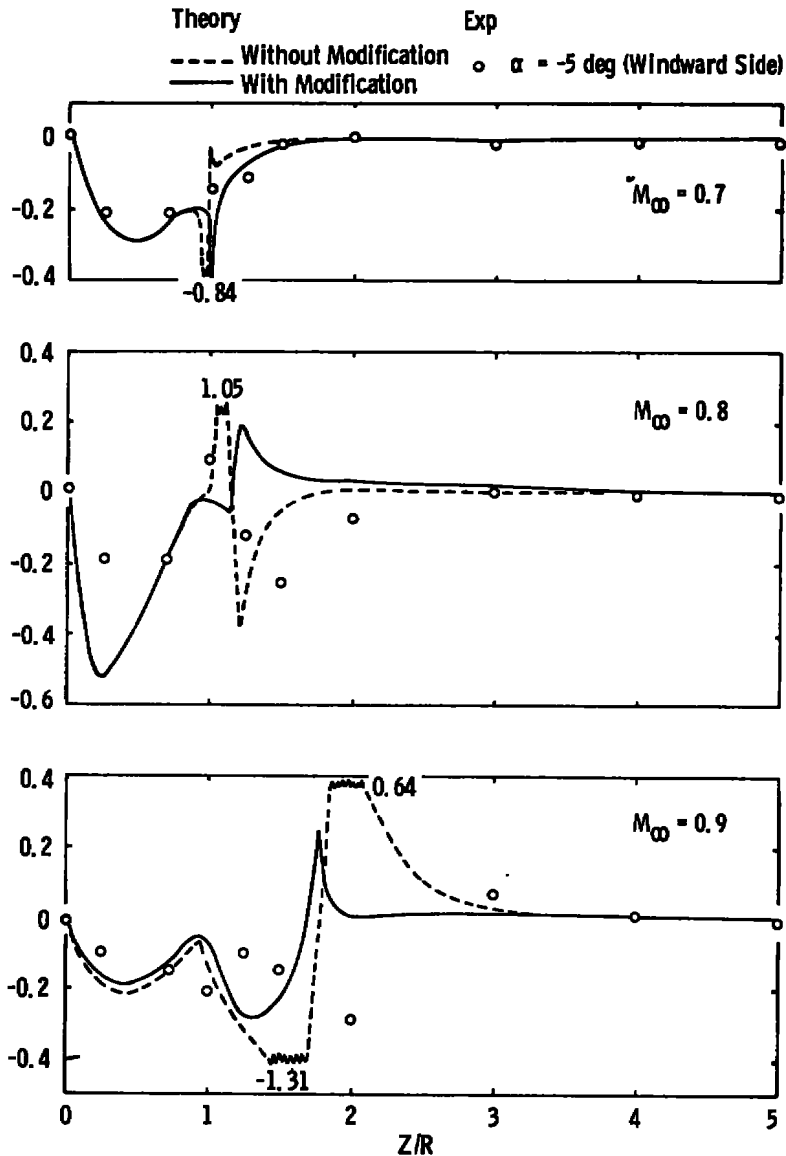
As described in Section 4.3.1, unrealistic spike was found at the region of embedded shock. South and Jameson used the criterion of minimum Laplacian ($\nabla^2 \phi_o$) to define the location of shock and smooth the flow field immediately upstream and downstream of the shock by one-sided extrapolation. In this section, the same one-sided extrapolation at the embedded shock is used for the quasi-steady flow solution, and the effect of the embedded shock on the solution of the perturbed flow field is examined. The cases examined are the 2:1 ellipse-nose-cylinder at $M_\infty = 0.9$ and the hemisphere-cylinder at $M_\infty = 0.7, 0.8$, and 0.9 . Significant changes are found in the pressure distribution near the embedded shock, as the following paragraph describes.

Theoretical results with and without modification are shown in Fig. 15 by solid and dashed curves, respectively. For the ellipse-nose-cylinder (Fig. 15a), the spike value is



a. Ellipse-cylinder, $M_\infty = 0.9$

Figure 15. Comparison of theoretical results with and without modification and experimental data.



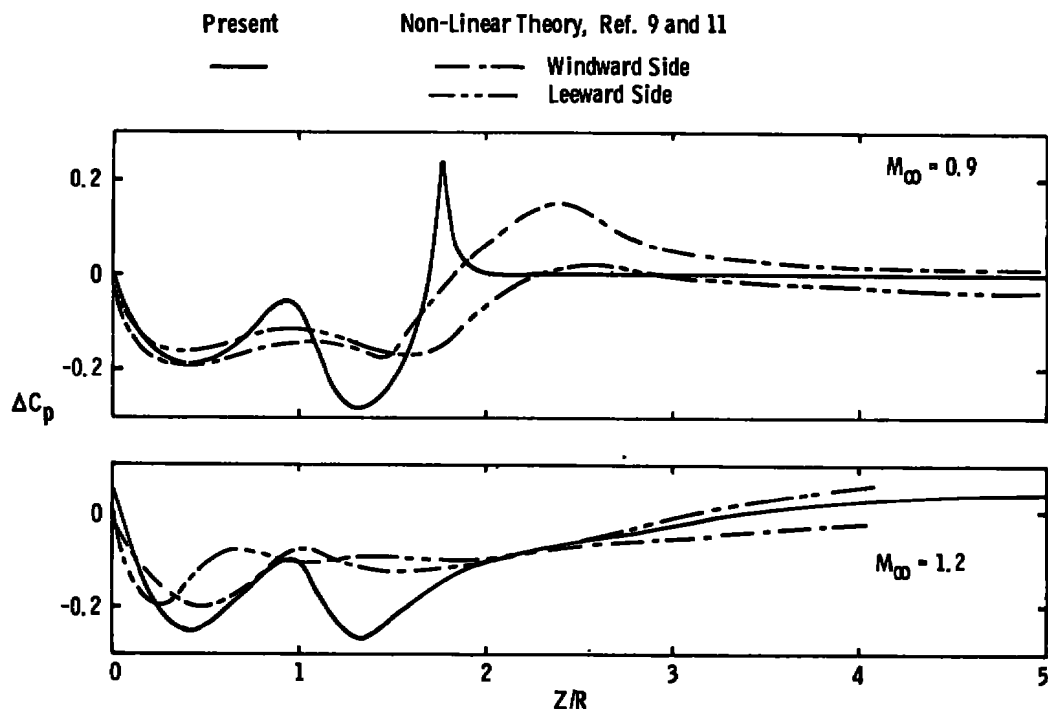
b. Hemisphere-cylinder
Figure 15. Concluded.

reduced from -4.31 to -1.8, approximately, and in the downstream of the shock, the perturbed pressure does not become positive, as shown by the previous result and the experimental data. Now, the theoretical result for $M_\infty = 0.9$ looks just like the other cases for $M_\infty \geq 1.0$. For the hemisphere-cylinder at $M_\infty = 0.7$, Fig. 15b, the spike value reduces from -0.84 to -0.4. The new results of surface pressure change significantly after modification at $M_\infty = 0.8$ and 0.9. At $M_\infty = 0.8$, the spike value of ΔC_p reduces from 1.05 to 0.2 and then monotonically approaches zero without the second spike in the

$-\Delta C_p$ side; and at $M_\infty = 0.9$, the spike at the $-\Delta C_p$ side disappears entirely while the positive side reduces from 0.64 to 0.24. The comparison between theory (after modification) and experiment is fair in the windward side except at $M_\infty = 0.8$ where flow separation prevails even at the windward side. From the above comparison, it is clear that the perturbed surface pressure obtained with modification at the embedded shock provides better solution. It should be pointed out that, although the present results differ significantly from the previous results in surface pressure distribution, the integrated aerodynamic coefficients change only slightly. Hence, the results reported in Section 4.3.3 remain unchanged.

4.3.5 Comparison with Nonlinear Theory

Inviscid nonlinear computations made by solving the Euler's equations are available for a hemisphere-cylinder at $\alpha = 5^\circ$ and $M_\infty = 1.2$ (Ref. 9) and $M_\infty = 0.9$ (Ref. 11). In Fig. 16a, the perturbed surface pressure distributions are compared between the



a. Quasi-steady perturbation pressure

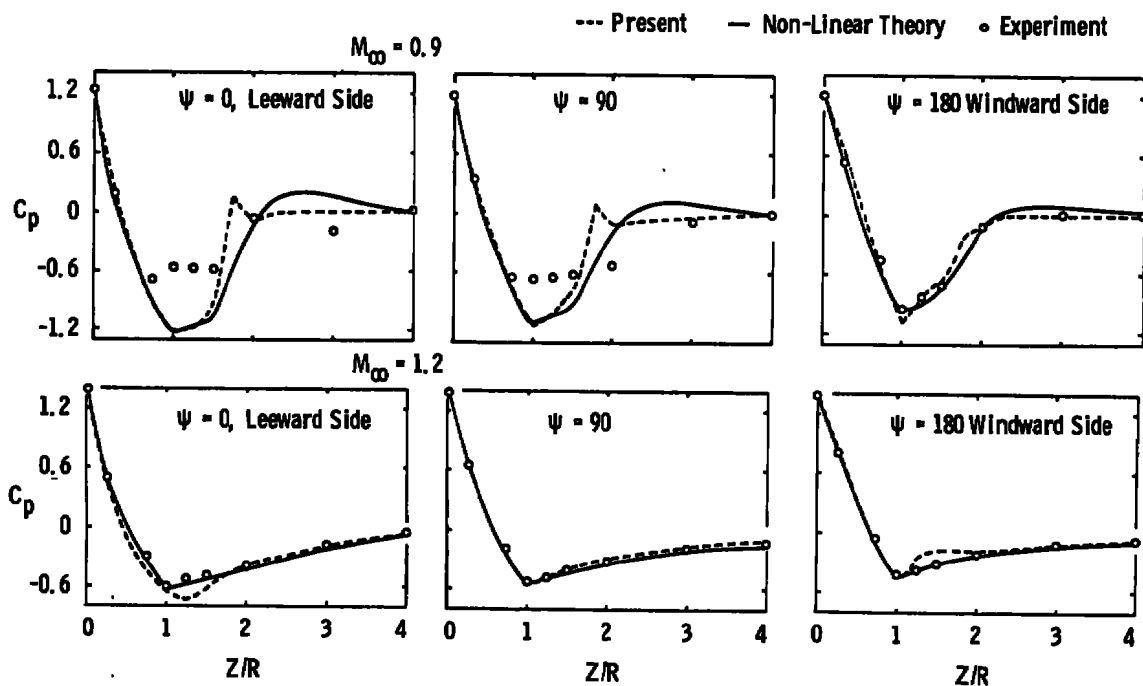
Figure 16. Comparison of perturbation theory with nonlinear (Euler's equations) theory for a hemisphere-cylinder at $\alpha = 5^\circ$ and $M_\infty = 0.9$ and 1.2.

nonlinear theory and the present method. Since in Ref. 11 only the C_p values at $\psi = 0$ deg, 90 deg, and 180 deg were given, the C_p values at $\psi = 90$ deg were used to replace C_p values at $\alpha = 0$ to obtain the perturbed surface pressure. That is,

$$\text{Windward side} \quad \Delta C_p = C_{p\psi=180^\circ} - C_{p\psi=90^\circ}$$

$$\text{Leeward side} \quad \Delta C_p = C_{p\psi=90^\circ} - C_{p\psi=0}$$

The ΔC_p curves between present calculation and the nonlinear theory agree well in the trend. It is also noted that at $\alpha = 5$ deg the assumption of $\cos \psi$ variation of flow variables in the present theory is perhaps invalid at the nose for $M_\infty = 1.2$ and at $1.5 < z/R < 3.0$ for $M_\infty = 0.9$.



b. Quasi-steady pressure
Figure 16. Concluded.

A plot of the total pressure C_p for a hemisphere-cylinder at $\alpha = 5$ deg and $\psi = 0, 90$, and 180 deg is shown in Fig. 16b for $M_\infty = 0.9$ and 1.2 . The agreement between present theory and the nonlinear theory is good except near the embedded shock region for $M_\infty = 0.9$ and aft of the juncture of the hemisphere and the cylinder for $M_\infty = 1.2$.

The experimental data at $\psi = 0$ and 90 deg for $M_\infty = 0.9$ clearly show that the flow is separated in these two meridian planes.

4.3.6 Unsteady Calculation

Unsteady calculations were first performed for a parabolic arc nose at a reduced frequency of $k = 0.006$ and $M_\infty = 1.0$. This case was computed by Liu and Ruo (Refs. 2 and 12) by extending the parabolic method of Oswatish and Keune (Ref. 13). The comparison of the stability derivatives of the total damping-in-pitch from the present theory and the theory of Liu and Ruo as well as the linearized theory of Landahl (Fig. 12 of Ref. 12) is shown in Fig. 17 for a variation in pitch center. The agreement between the

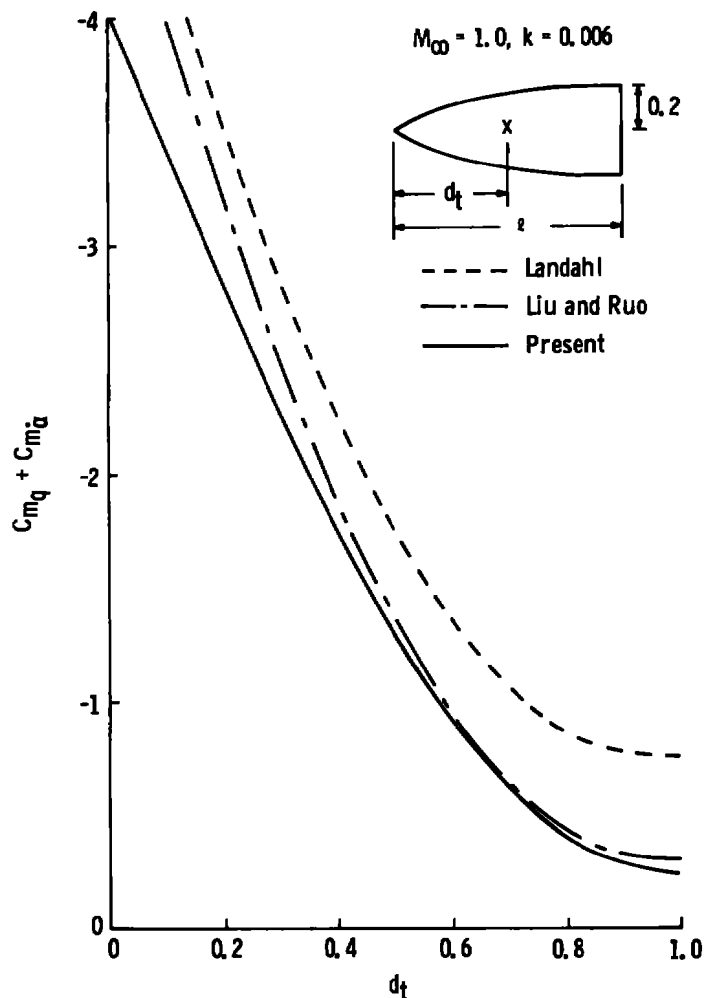


Figure 17. Comparison of theoretical stability derivatives for a parabolic arc nose.

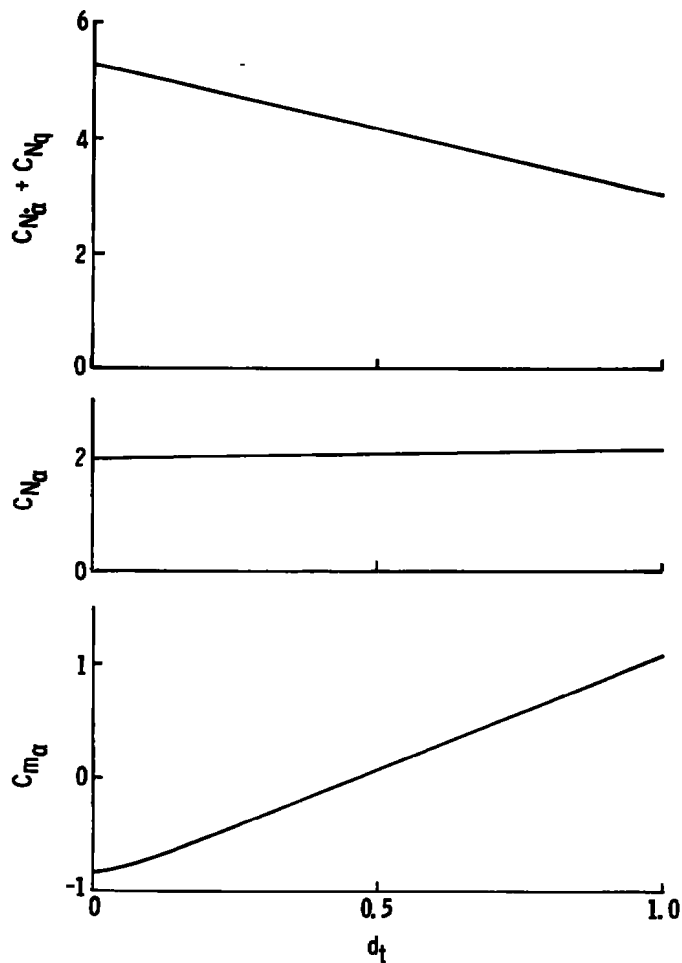


Figure 17. Concluded.

present theory and that of Liu and Ruo is good except for $d_t \rightarrow 0$, where the present theory gives a lower value. It should be noted that Landahl's linearized theory is invalid for such a low reduced frequency. Liu's theory indicates a reduction of the total damping-in-pitch coefficient when the nonlinearity of the differential equation is approximately accounted for. The present theory indicates that if the nonlinearity is fully accounted for, the total damping-in-pitch coefficient is even lower. No experimental data are available for comparison. Other stability derivatives such as $C_{N_{\dot{\alpha}}} + C_{N_q}$, $C_{N_{\alpha}}$, and $C_{m_{\alpha}}$ calculated by the present method as a function of d_t are also shown in Fig. 17. Again, no data are available for comparison for these quantities.

No transonic unsteady surface pressure measurements for a body of revolution have been reported in the literature. Therefore, a comparison of the unsteady surface pressure

is not available. However, a stability derivative for total damping-in-pitch, $C_{m_{\dot{\alpha}}} + C_{m_q}$, has been reported in Refs. 14 and 15 for a 2-caliber ogive-nose-cylinder and a hemisphere-cylinder. In these measurements, the models were pitched at a constant frequency of 36 Hz; hence the reduced frequency changes with the free-stream Mach number as follows:

$\frac{M_\infty}{k} =$	0.6	0.7	0.8	0.9	1.0	1.1	1.2
$k =$	0.0165	0.0145	0.0124	0.0112	0.0099	0.0095	0.0088

Calculations were made using the corresponding reduced frequency for each Mach number. Figure 18 shows the stability derivatives for total damping-in-pitch for the ogive-cylinder. The $C_{m_{\dot{\alpha}}} + C_{m_q}$ value given by the theory is generally higher than the experimental data, particularly for the lower Mach number. No data are available for comparison for $C_{N_{\dot{\alpha}}} + C_{N_q}$.

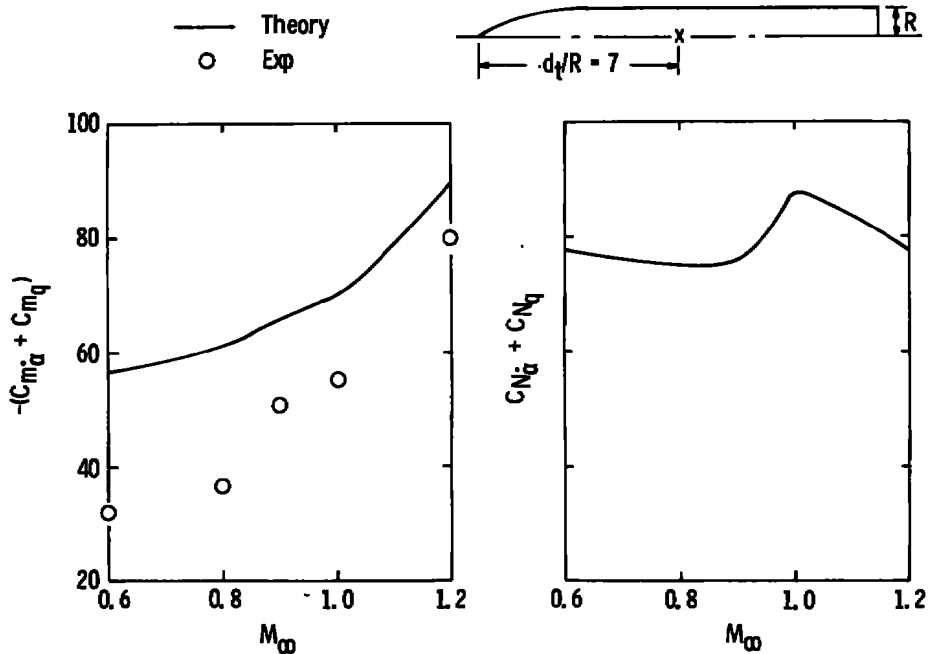


Figure 18. Comparison of dynamic stability derivatives between theory and experiments for a 2-caliber ogive-nose-cylinder.

For the hemisphere-cylinder, the comparison between theory and experiments is shown in Fig. 19 for two pitch centers. The experimental data for $d_t/R = 7$ were obtained from Ref. 13 for the full span model; data for $d_t/R = 5$ and 6 are from Ref. 14. The agreement between theory and experiment is fair. The theoretical calculations were made

for $M_\infty = 0.6, 0.7, 0.8, 0.9, 1.0$, and 1.2 to determine the curves, which at first look do not show the trend given by the experimental data for $d_t/R = 5$ and 7 . However, the experiments for $d_t/R = 7$ gave a positive value of $C_{m\dot{\alpha}} + C_{m\dot{q}}$ (unstable) at $M_\infty = 0.9$, which was not predicted by the theory, and the set of data for $d_t/R = 5$ also indicate a drop of $C_{m\dot{\alpha}} + C_{m\dot{q}}$ at $M_\infty = 1.4$. When these characteristics of the experimental data are considered, the theoretical curves do not seem unreasonable. In addition, the experimental data for the $d_t/R = 6$ set behaved differently from the other sets. Hence, perhaps one needs more experimental data in the Mach number range shown in Fig. 19 in order to fully evaluate the theoretical results. As pointed out previously, for a hemisphere-cylinder in the transonic flow regime, the flow field is complicated by the viscous and inviscid interaction. Therefore, inviscid theory may not be sufficient to predict the dynamic stability derivatives. Theoretical values for $C_{N\dot{\alpha}} + C_{N\dot{q}}$ are also plotted in Fig. 19.

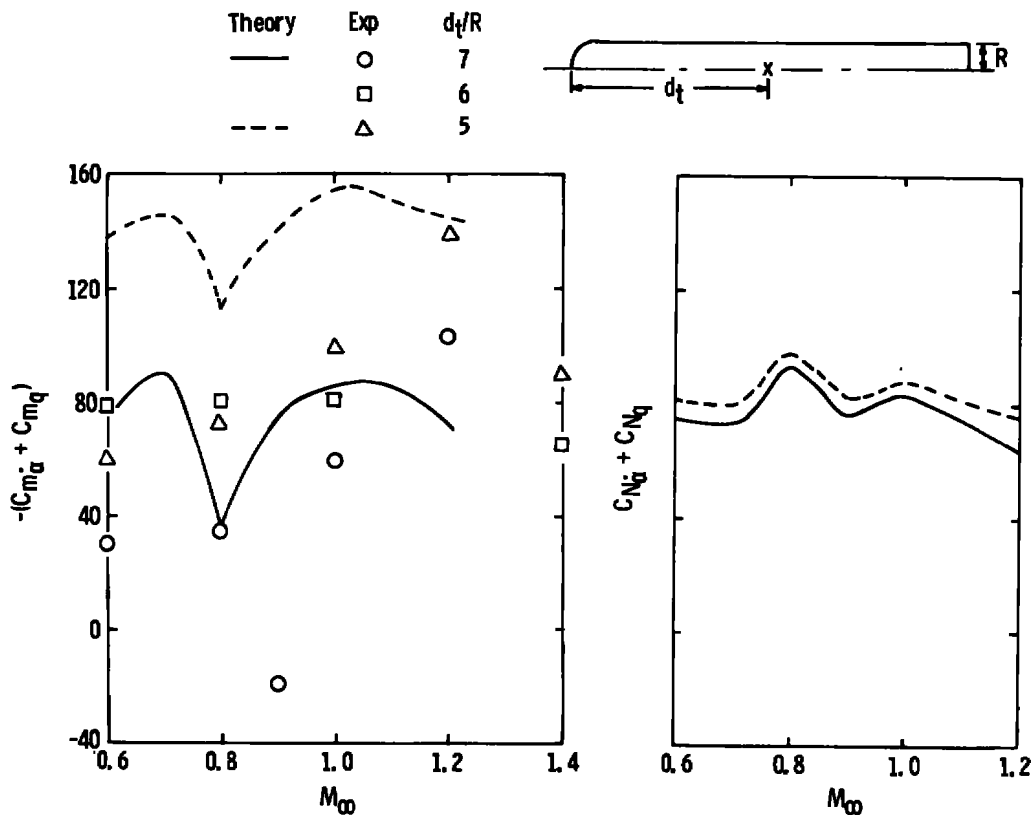


Figure 19. Comparison of dynamic stability derivatives between theory and experiments for a hemisphere-cylinder.

5.0 CONCLUDING REMARKS

A perturbation theory and numerical solution, based on the unsteady full potential equation, were developed for unsteady transonic flow about blunt and pointed bodies of revolution undergoing harmonic oscillations. The oscillatory motion was considered to be a small perturbation of the nonlinear steady flow. The coupled equations for the steady and unsteady potentials were solved numerically using a rotating difference scheme. Calculations were performed for ogive-cylinder, ellipse-cylinder, hemisphere-cylinder, and parabolic arc nose shapes undergoing pulsatile and pitching oscillations. Comparisons of the present theory with available experiments and other theories are presented for the surface pressure distribution at quasi-steady state and for the static and dynamic stability derivatives. The agreement is good for the quasi-steady cases.

REFERENCES

1. Landahl, M. T. Unsteady Transonic Flow. Pergamon Press, New York, 1961.
2. Liu, D. D., Platzler, M. F., and Ruo, S. Y. "Unsteady Linearized Transonic Flow Analysis for Slender Bodies." AIAA Journal, Vol. 15, No. 7, July 1977, pp. 966-973.
3. Kimble, K. R., Liu, D. D., Ruo, S. Y., and Wu, J. M. "Unsteady Transonic Flow Analysis for Low Aspect Ratio, Pointed Wings." AIAA Journal, Vol. 12, No. 4, April 1974, pp. 516-522.
4. Stahara, S. S. and Spreiter, J. R. "Unsteady Local Linearization Solution for Pitching Bodies of Revolution at Freestream Mach Numbers = 1: Stability Derivative Analysis." AIAA Journal, Vol. 14, No. 10, October 1976, pp. 1402-1408.
5. South, J. and Jameson, A. "Relaxation Solution for Inviscid Axisymmetric Transonic Flow over Blunt or Pointed Bodies." Proceedings of AIAA Computational Fluid Dynamics Conference, July 19-20, 1973.
6. Hsieh, T. "Flow Field Study about a Hemispherical Cylinder in Transonic and Low Supersonic Mach Number Range." AIAA Paper 75-83, January 1975.
7. Pai, S. I. Introduction to the Theory of Compressible Flow. Van Nostrand Company, Inc., Princeton, N. J., 1959.
8. Hartley, M. S. and Jacocks, J. L. "Static Pressure Distributions on Various Bodies of Revolution at Mach Numbers from 0.60 to 1.60." AEDC-TR-68-37 (AD828571), March 1968.

9. Hsieh, T. "An Investigation of Separated Flow about a Hemisphere-Cylinder at 0- to 19-deg Incidence in the Mach Number Range from 0.6 to 1.5." AEDC-TR-76-112, November 1976.
10. Anderson, C. F. and Henson, J. R. "Aerodynamic Characteristics of Several Bluff Bodies of Revolution at Mach Numbers from 0.6 to 1.5." AEDC-TR-71-130. (AD885911), July 1971.
11. Pulliam, T. H. and Steger, J. L. "On Implicit Finite-Difference Simulations of Three-Dimensional Flow." AIAA Paper No. 78-10, January 1978.
12. Ruo, S. Y. and Liu, D. D. "Calculation of Stability Derivatives for Slowly Oscillating Bodies of Revolution at Mach 1.0." HREC-0082-24, February 1971.
13. Oswatish, K. and Keune, F. "Flow Around Bodies of Revolution at Mach Number One." Proceedings of the Conference on High-Speed Aeronautics, Polytechnic Institute of Brooklyn, 20-22 January 1955, ed. Antonio Ferri, et al.
14. Shadow, T. O. "An Investigation of the Half-Model Reflection-Plane Technique for Dynamic Stability Testing at Transonic Mach Numbers." AEDC-TR-76-165 (ADA035567), January 1977.
15. Shadow, T. O. and Paulk, R. A. "Dynamic Stability Characteristics of Bluff Bodies of Revolution at Transonic Mach Numbers." AEDC-TR-72-110 (AD902214L), August 1972.

APPENDIX A **DIFFERENCE FORM OF TERMS IN EQ. (18)**

The difference form of each term involved in arriving at Eqs. (20), (21), and (22) is given below.

I. For the $\partial^2/\partial S^2$ term

A. If $(1 - q_0^2/a_0^2) > 0$

$$\begin{aligned}
 Q \left(\phi_{1R_{SS}} \right)_{i,j} &= Q \frac{1}{\Delta r^2} \left(\frac{U_o^2}{q_o^2} \right)_{i,j} \left[\left(\frac{f}{H} \right)_i \left(\frac{f}{H} \right)_{i-\frac{1}{2},j} \left(\phi_{1R_{i+1,j}} - \phi_{1R_{i,j}} \right) \right. \\
 &\quad \left. - \left(\frac{f}{H} \right)_{i-\frac{1}{2},j} \left(\phi_{1R_{i,j}} - \phi_{1R_{i-1,j}} \right) \right] \\
 &+ Q \frac{1}{2\Delta r \Delta \zeta} \left(\frac{V_o U_o}{q_o^2} \right)_{i,j} \left(\frac{f}{H} \right)_i g_j \left[\phi_{1R_{i+1,j-1}} - \phi_{1R_{i-1,j-1}} \right. \\
 &\quad \left. - \phi_{1R_{i+1,j+1}} + \phi_{1R_{i-1,j+1}} \right] + Q \frac{1}{\Delta \zeta^2} \left(\frac{V_o^2}{q_o^2} \right)_{i,j} \\
 &g_i \left[g_{i-\frac{1}{2}} \left(\phi_{1R_{i,j-1}} - \phi_{1R_{i,j}} \right) - g_{j+\frac{1}{2}} \left(\phi_{1R_{i,j}} - \phi_{1R_{i,j+1}} \right) \right] \\
 &= \beta_1 \phi_{1R_{i-1,j-1}} + \beta_2 \phi_{1R_{i,j-1}} + \beta_3 \phi_{1R_{i+1,j-1}} + \beta_4 \phi_{1R_{i+1,j}} \\
 &\quad + \beta_5 \phi_{1R_{i,j}} + \beta_6 \phi_{1R_{i-1,j}} + \beta_7 \phi_{1R_{i-1,j+1}} + \beta_8 \phi_{1R_{i,j+1}} \\
 &\quad + \beta_9 \phi_{1R_{i+1,j+1}}
 \end{aligned} \tag{A-1}$$

where

$$\beta_1 = -\beta_3 = -\beta_7 = \beta_9 = -a_2 Q$$

$$\beta_2 = a_3 g_{j-\frac{1}{2}} Q$$

$$\beta_4 = a_1 \left(\frac{f}{H} \right)_{i-\frac{1}{2},j} Q$$

$$\beta_5 = a_1 \left[\left(\frac{f}{H} \right)_{i-\frac{1}{2},j} + \left(\frac{f}{H} \right)_{i+\frac{1}{2},j} \right] Q - a_3 \left(g_{i-\frac{1}{2}} + g_{j+\frac{1}{2}} \right)$$

$$\beta_6 = a_1 \left(\frac{f}{H} \right)_{i-\frac{1}{2},j} Q$$

$$\beta_8 = a_3 g_{j+\frac{1}{2}} Q$$

$$a_1 = \frac{1}{\Delta r^2} \left(\frac{U_o^2}{q_o^2} \right)_{i,j} \left(\frac{f}{H} \right)_{i,j}$$

$$a_2 = \frac{1}{2\Delta r\Delta \zeta} \left(\frac{V_o U_o}{q_o^2} \right)_{i,j} \left(\frac{f}{H} \right)_{i,j} q_j$$

$$a_3 = \frac{1}{\Delta \zeta^2} \left(\frac{V_o^2}{q_o^2} \right)_{i,j} g_j$$

where the terms Δr and $\Delta \zeta$ are the mesh spacing in the computational plane, Fig. 2. The terms f and g are the stretching function in the s and n directions. The expression H is defined in Fig. 1, and the terms i and j are the grid points along the s and n directions, respectively.

B. If $(1 - q_o^2/a_o^2) < 0$

1. When $V_o > 0$

$$\begin{aligned} Q (\phi_{1R_{SS}})_{i,j} &= \frac{Q}{\Delta r^2} \left(\frac{U_o^2}{q_o^2} \right)_{i,j} \left[\left(\frac{f}{H} \right)_{i-\frac{1}{2},j} (\phi_{1R_{i,j}} - \phi_{1R_{i-1,j}}) \right. \\ &\quad \left. - \left(\frac{f}{H} \right)_{i-\frac{3}{2},j} (\phi_{1R_{i-1,j}} - \phi_{1R_{i-2,j}}) \right] \\ &\quad + \frac{Q}{\Delta r\Delta \zeta} \left(\frac{2U_o V_o}{q_o^2} \right)_{i,j} \left(\frac{f}{H} \right)_{i-\frac{1}{2},j+\frac{1}{2}} g_{j+\frac{1}{2}} \left[\phi_{1R_{i,j}} - \phi_{1R_{i-1,j}} \right] \end{aligned}$$

$$\begin{aligned}
& - \phi_{1R_{i,j+1}} + \phi_{1R_{i-1,j+1}} \Big] \\
& + \frac{Q}{\Delta \zeta^2} \left(\frac{v_o^2}{q_o^2} \right)_{i,j} g_{j+1} \left[g_{j+\frac{1}{2}} \left(\phi_{1R_{i,j}} - \phi_{1R_{i,j+1}} \right) \right. \\
& \quad \left. - g_{j-\frac{3}{2}} \left(\phi_{1R_{i,j+1}} - \phi_{1R_{i,j+2}} \right) \right] \\
& = \gamma_1 \phi_{1R_{i-2,j}} + \gamma_2 \phi_{1R_{i-1,j}} - \gamma_3 \phi_{1R_{i,j}} + \gamma_4 \phi_{1R_{i-1,j+1}} \\
& \quad + \gamma_5 \phi_{1R_{i,j+1}} + \gamma_6 \phi_{1R_{i,j+2}}
\end{aligned} \tag{A-2}$$

where

$$\begin{aligned}
\gamma_1 &= b_1 \left(\frac{f}{H} \right)_{i-\frac{3}{2},j} Q \\
\gamma_2 &= -b_1 \left[\left(\frac{f}{H} \right)_{i-\frac{1}{2},j+\frac{1}{2}} + \left(\frac{f}{H} \right)_{i-\frac{3}{2},j+\frac{1}{2}} \right] Q - b_2 Q \\
\gamma_3 &= \left[b_1 \left(\frac{f}{H} \right)_{i-\frac{1}{2},j} + b_2 + b_3 g_{j+\frac{1}{2}} \right] Q \\
\gamma_4 &= b_2 Q \\
\gamma_5 &= - \left[b_2 + b_3 \left(g_{i+\frac{1}{2}} + g_{j+\frac{3}{2}} \right) \right] Q \\
\gamma_6 &= b_3 g_{j-\frac{3}{2}} Q \\
b_1 &= \frac{1}{\Delta r^2} \left(\frac{u_o^2}{q_o^2} \right)_{i,j} \left(\frac{f}{H} \right)_{i-1,j} \\
b_2 &= \frac{1}{\Delta r \Delta \zeta} \left(\frac{2u_o v_o}{q_o^2} \right) \left(\frac{f}{H} \right)_{i-\frac{1}{2},j+\frac{1}{2}} g_{j+\frac{1}{2}} \\
b_3 &= \frac{1}{\Delta \zeta^2} \left(\frac{v_o^2}{q_o^2} \right)_{i,j} g_{j+1}
\end{aligned}$$

2. When $V_o \leq 0$ or on the boundary, $j = J$ (see Fig. 3)

$$Q (\phi_{1R_{ss}})_{i,j} = \gamma'_1 \phi_{1R_{i-2,j}} + \gamma'_2 \phi_{1R_{i-1,j}} + \gamma'_3 \phi_{1R_{i,j}} \\ + \gamma'_4 \phi_{1R_{i-1,j-1}} + \gamma'_5 \phi_{1R_{i,j-1}} - \gamma'_6 \phi_{1R_{i,j-2}} \quad (A-3)$$

where

$$\gamma'_1 = \gamma_1 \\ \gamma'_2 = -b_1 \left[\left(\frac{f}{H} \right)_{i-\frac{1}{2},j-\frac{1}{2}} + \left(\frac{f}{H} \right)_{i-\frac{3}{2},j-\frac{1}{2}} \right] Q - b'_2 Q \\ \gamma'_3 = \left[b_1 \left(\frac{f}{H} \right)_{i-\frac{1}{2},j} + b'_2 + b'_3 g_{j-\frac{1}{2}} \right] Q \\ \gamma'_4 = b'_2 Q \\ \gamma'_5 = - \left[b'_2 + b'_3 \left(g_{j-\frac{1}{2}} + g_{j-\frac{3}{2}} \right) \right] Q \\ \gamma'_6 = b'_3 g_{j-\frac{3}{2}} Q \\ b'_2 = \frac{1}{\Delta r \Delta \zeta} \left(\frac{2U_o V_o}{q_o^2} \right) \left(\frac{f}{H} \right)_{i-\frac{1}{2},j-\frac{1}{2}} g_{j-\frac{1}{2}} \\ b'_3 = \frac{1}{\Delta \zeta^2} \left(\frac{V_o^2}{q_o^2} \right)_{i,j} j g_{j-1}$$

II. For the $\partial^2/\partial N^2$ term

This term is independent of the local flow condition, or

$$(\phi_{1R})_{NN} = \frac{1}{\Delta r^2} \left(\frac{V_o^2}{q_o^2} \right)_{i,j} \left(\frac{f}{H} \right)_{i,j} \left[\left(\frac{f}{H} \right)_{i+\frac{1}{2},j} (\phi_{1R_{i+1,j}} - \phi_{1R_{i,j}}) \right. \\ \left. - \left(\frac{f}{H} \right)_{i-\frac{1}{2},j} (\phi_{1R_{i,j}} - \phi_{1R_{i-1,j}}) \right]$$

$$\begin{aligned}
& - \frac{1}{2\Delta\tau\Delta\zeta} \left(\frac{V_o U_o}{q_o^2} \right)_{i,j} \left(\frac{f}{H} \right)_{i,j} g_j \left(\phi_{1R_{i+1,j-1}} - \phi_{1R_{i-1,j-1}} \right. \\
& \quad \left. - \phi_{1R_{i+1,j+1}} + \phi_{1R_{i-1,j+1}} \right) \\
& + \frac{1}{\Delta\zeta^2} \left(\frac{U_o^2}{q_o^2} \right)_{i,j} g_j \left[g_{j-\frac{1}{2}} \left(\phi_{1R_{i,j-1}} - \phi_{1R_{i,j}} \right) \right. \\
& \quad \left. - g_{j+\frac{1}{2}} \left(\phi_{1R_{i,j}} - \phi_{1R_{i,j+1}} \right) \right] \\
& = a_1 \phi_{1R_{i-1,j-1}} - a_2 \phi_{1R_{i,j-1}} + a_3 \phi_{1R_{i+1,j-1}} \\
& + a_4 \phi_{1R_{i+1,j}} + a_5 \phi_{1R_{i,j}} + a_6 \phi_{1R_{i-1,j}} + a_7 \phi_{1R_{i-1,j+1}} \\
& + a_8 \phi_{1R_{i,j+1}} + a_9 \phi_{1R_{i+1,j+1}}
\end{aligned} \tag{A-4}$$

where

$$\begin{aligned}
a_1 &= -a_3 = -a_7 = a_9 = a_2 \\
a_2 &= a_3 g_{i,j-\frac{1}{2}} \\
a_4 &= a_1 \left(\frac{f}{H} \right)_{i+\frac{1}{2},j} \\
a_5 &= -a_1 \left[\left(\frac{f}{H} \right)_{i+\frac{1}{2},j} + \left(\frac{f}{H} \right)_{i-\frac{1}{2},j} \right] - a_3 g_{j-\frac{1}{2}} + g_{j+\frac{1}{2}} \\
a_6 &= a_1 \left(\frac{f}{H} \right)_{i-\frac{1}{2},j} \\
a_8 &= a_3 g_{j+\frac{1}{2}} \\
a_1 &= \frac{1}{\Delta\tau^2} \left(\frac{V_o^2}{q_o^2} \right)_{i,j} \left(\frac{f}{H} \right)_{i,j} \\
a_2 &= \frac{1}{2\Delta\tau\Delta\zeta} \left(\frac{V_o U_o}{q_o^2} \right)_{i,j} \left(\frac{f}{H} \right)_{i,j} g_j
\end{aligned}$$

$$a_3 = \frac{1}{\Delta \zeta^2} \left(\frac{1 \cdot 2}{q_o^2} \right)_{i,j} g_i$$

The rest of the terms in Eq. (18) may be written as follows:

$$\frac{C_4}{H} \cdot \frac{\partial \phi_{1R}}{\partial s} = C_4' \left(\phi_{1R_{i+1,j}} - \phi_{1R_{i-1,j}} \right) \quad (A-5)$$

$$C_5 \frac{\partial \phi_{1R}}{\partial n} = C_5' \left(\phi_{1R_{i,j-1}} - \phi_{1R_{i,j+1}} \right) \quad (A-6)$$

$$\frac{C_6}{H} \frac{\partial \phi_{1I}}{\partial s} = C_6' \left(\phi_{1I_{i+1,j}} - \phi_{1I_{i-1,j}} \right) \quad (A-7)$$

$$C_7 \frac{\partial \phi_{1I}}{\partial n} = C_7' \left(\phi_{1I_{i,j-1}} - \phi_{1I_{i,j+1}} \right) \quad (A-8)$$

$$C_8 \phi_{1R} = C_8 \phi_{1R_{i,j}} \quad (A-9)$$

NOMENCLATURE

a	Speed of sound
A_i, B_i, C_i	Coefficients
a_i, b_i, c_i	Coefficients
\bar{B}	Equation for the boundary, Eq. (12)
$C_{A,F}$	Forebody axial-force coefficient, F_A/q
$C_{N_\alpha}, C_{m_\alpha}$	Stability derivative caused by angle of attack
$C_{N_{\dot{\alpha}}} + C_{N_q}, C_{m_{\dot{\alpha}}} + C_{m_q}$	Stability derivative caused by total damping-in-pitch
C_p	Pressure coefficient, $(p - p_\infty)/q$
ΔC_p	Perturbed pressure coefficient, p_1/q
$\overline{\Delta C_p}$	Average perturbed pressure coefficient, Eq. (37)
d_t	Pitching center from the nosetip
F_A	Axial force on forebody
H	$(1 - n \, ds/d\theta)$
h_o	Amplitude of harmonically heaving oscillation
I, J	Maximum grid index along the s and n directions, respectively
K	Curvature of body meridian plane, $-d\theta/ds$
k	Reduced frequency, $\omega R/U_\infty$
ℓ	Total length of the body
M	Mach number
n, s	Body normal and tangent coordinates

n_1	Perturbed body boundary due to motion
p	Pressure
Δp	Perturbed pressure
Q	$(1 - q_0^2/a_0^2)$
q	Dynamic pressure, $1/2 \rho_\infty U_\infty^2$
\bar{q}	Velocity vector
R	Radius of the cylindrical body
R_t	Radius of the expanded or shrunken cylindrical body
r, z	Radial and axial coordinates
t	Time
U, V, W	Axial, vertical, and circumferential velocity components, respectively
X, Y, Z	Cartesian coordinates
$X_{N,P}$	Aerodynamic moment center or neutral point of pitching moment, positive forward of body mid-point, $(C_{M_\alpha}/C_{n_\alpha})_{mid-point}$
α	Angle of attack
$\alpha_i, \beta_i, \gamma_i$	Coefficients
γ	Gas constant
δ_0	Amplitude of harmonically pulsatile oscillation
ξ, τ	Computational coordinates
θ	Slope of body geometry in the meridian plane
μ	Dynamic viscosity of the fluid
ρ	Density of the fluid
τ_0	Amplitude of harmonically pitching oscillation

ϕ	Velocity potential
ψ	Circumferential angle starting from lee-side plane of symmetry
ω	Oscillation frequency, cycle/sec

SUBSCRIPTS

0,1	Steady and perturbed unsteady components, respectively
i,j	Index along the body and normal coordinates, respectively
I,R	Imaginary and real parts, respectively
∞	Free stream

THREE DIMENSIONAL THERMAL ANALYSIS OF MK. 82 TYPE.

* IS PBM. ON 6600 ?

AD 142374 AFAC TR 57-112 (Influ. of Prob. of Temp. & Press. Inf. the Design of Bomb Components)

AD 142377 AFAC TR 57-112. (II)

AD 142378 (III)

AD 142391 (IV)

CAF 33(616)-3030

Nov. 57

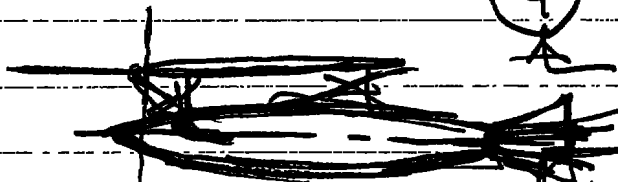
AFATL TR 70-5 Vol. I ADV. ORD. THERMAL ANALYSIS.

$h = 90.646''$

T_n
 q

1. Recovery Temp. & Schlieren
2. Heat transfer studies.

P



Orientation? of Bomb & Wind.

$M = 1.89$

$= 2.25$

$= 3.0$